UNIVERSITY OF CALIFORNIA
RIVERSIDE

Development and Application of Optical Coherence Tomography for Detection of Cerebral Edema *in Vivo*

A Dissertation submitted in partial satisfaction
of the requirements for the degree of

Doctor of Philosophy

in

Bioengineering

by

Carissa Lynne Rodriguez

August 2015

Dissertation Committee:

Dr. B. Hyle Park, Chairperson
Dr. Devin Binder
Dr. Todd Fiacco

The Dissertation of Carissa Lynne Rodriguez is approved:

Committee Chairperson

University of California, Riverside

ACKNOWLEDGEMENTS

Numerous people have supported me throughout the process of the research and writing of this dissertation. First, I would like to thank my advisor, Dr. Hyle Park, for his guidance and mentorship over the past five years. He has always been willing to help me reason through the answers to any questions I had, always available to listen to my ideas and thoughts on the trajectory of our research and always willing to provide feedback on presentations and written work. I am grateful for the dedication he shows to his students' professional development and research. This work would not have been possible without his continued guidance and support. It has been a joy and an honor to work in his lab.

I would also like to express my gratitude to the members of my dissertation committee, Dr. Devin Binder and Dr. Todd Fiacco. Dr. Binder has collaborated with me on this project since its inception and provided me with continual guidance. His biological expertise and valuable clinical experience has helped shape this work and I am very appreciative of his support and feedback over the years. Dr. Fiacco, who has served on my dissertation committee and my candidacy committee, has also provided valuable advice throughout the completion of this project and I am grateful for the guidance he has provided.

Additionally I would like to thank the numerous other faculty members who have contributed to my progress and success. Thank you to Dr. Dimitrios Morikis and Dr. Victor Rodgers, who both served on my candidacy committee. They provided unique insight into my project and steadfast support throughout my time here. Thank you to Dr.

Bir Bhanu and the other faculty advisors of the National Science Foundation Integrative Graduate Education, Research and Training (IGERT) program in video bioinformatics for accepting me into the program and providing me with financial support during my last two years. I am extremely grateful to have had the opportunity to participate in this interdisciplinary program and it will have a lasting impact throughout my career.

I also want to thank all of the past and present members of the Neuroscience and Optical Imaging Research group at the University of California Riverside (UCR). Melissa Eberle has been a great friend and colleague during my time at UCR. We started in the lab at the same time and worked on much of the early stages of this project together. Whether it was problems with experiments or with Matlab not doing exactly what I wanted it to do, she was always there, sitting right across from me, to lift my spirits and motivate me to get back to it! We have shared the ups and downs of graduate school and I know this journey would have been much harder (and probably more boring) had she not been by my side. I want to thank Dr. Yan Wang, Dr. Shahid Islam and Christian Oh for their early work in building the OCT system and helping me as I started in the lab. I also want to thank Christian Oh for his help with the design and alignment of the differential absorption OCT system. Also, thank you to Dr. Michael Oliveira, Dr. Rezuanul Haque, Koji Hirota, Masum Hasan, Minh Tong and Danielle Ornelas for their help and support during my time here.

Additionally, I would like to acknowledge the members of Dr. Binder's lab for the assistance with our *in vivo* experiments. Thank you especially to Jenny Szu for not only helping me with countless *in vivo* experiments, but also for being willing to try new

ideas, for always making time for “just one more” experiment and for helping with many hours of data processing. She has been a great friend and colleague and her assistance made much of this work possible. I would also like to acknowledge Dr. Sandeep Dhall and Dr. Manuela Martins-Green for their collaboration in a side project in which we studied wound healing following burn injury.

I would like to thank my family, especially my parents and sister, for their continued love and support while I pursue my goals. I appreciate all the care and encouragement that they have given to me throughout my entire life and I am grateful that they have always supported my ambitions, even when it meant moving across the country.

Lastly, thank you to my wonderful husband, who has been by my side every step of the way. I could not have done this without his daily love, support and friendship.

I would also like to acknowledge the Journal of Neurophotonics for permission to use portions of work published in their journal in Chapter 2 of this dissertation (Neurophotonics, 2014 1(2), 025004) . Thank you to the Journal of Biomedical Optics for permission to use material that appeared in Journal of Biomedical Optics, 2015 20 (4) presented here in Appendix B. I would also like to acknowledge the funding sources that contributed to this work, which include the UC Discovery Grant 213073, NIH R00EB007241, NIHK08NS059674, NIHR01NS081243, seed funding from the UCR Office of Research and Development, UCR graduate research mentoring fellowship UCR dissertation year fellowship and NSF IGERT fellowship DGE 090366.

ABSTRACT OF THE DISSERTATION

Development and Application of Optical Coherence Tomography for Detection of Cerebral Edema *in Vivo*

by

Carissa Lynne Rodriguez

Doctor of Philosophy, Graduate Program in Bioengineering
University of California, Riverside, August 2015
Dr. B. Hyle Park, Chairperson

Cerebral edema is a condition characterized by a net increase in brain water content. Typically water content is tightly regulated in the brain. However this balance can be disrupted by a number of conditions including traumatic brain injury (TBI), tumor and ischemia and lead to brain swelling, raised intracranial pressure (ICP) and secondary damage that greatly increases the morbidity and mortality associated with these conditions. Intracranial pressure is the most common method for detecting and monitoring cerebral edema *in vivo*. However, this technique is only capable of providing a global assessment of brain water content and is unable to detect cerebral edema early in its development. The goal of the work presented here is to develop optical coherence tomography (OCT) as a tool for detecting cerebral edema *in vivo.* OCT is an optical imaging modality capable of producing cross-sectional images of biological samples with micrometer resolution. This work begins by studying an *in vivo* global edema model

with OCT and analyzing the change in the depth-resolved attenuation coefficient. Results demonstrated that the attenuation coefficient decreases due to edema. Additionally, decreased blood flow caused by severe brain swelling was also observed. Next, a focal model of edema is explored in a TBI mouse model. Scattering changes correlated with bleeding and edema formation were observed around the impact site. Lastly, OCT system modifications are described for creating a differential absorption-OCT system designed to increase the OCT signal sensitivity to water in particular, by using the absorption properties of water to determine local water content in the tissue. Preliminary results are presented. Overall the results of this work demonstrate that OCT is sensitive to changes in scattering and absorption caused by cerebral edema and highlight the potential of OCT for *in vivo* cerebral edema detection and monitoring in a spatially resolved manner.

Table of Contents

List of Figures

List of Acronyms

BBB: blood brain barrier
BWC: brain water content
CCI: controlled cortical impact
CT: computed tomography
DAI: diffuse axonal injury
DA-OCT: differential absorption-OCT
DOCT: Doppler OCT
DTI: diffusion tensor imaging
fMRI: functional MRI
FWHM: full width half maximum
GCS: Glasgow coma scale
ICP: intracranial pressure
IP: intraperitoneal
MIP: maximum intensity projection
MRI: magnetic resonance imaging
MRS: magnetic resonance spectroscopy
mTBI: mild traumatic brain injury
OCT: optical coherence tomography
PBS: phosphate buffered saline
PBS: polarizing beam splitter
PNS: peripheral nervous system
PSF: point spread function
PS-OCT: polarization-sensitive OCT
ROI: region of interest
SD-OCT: spectral domain-OCT
TBI: traumatic brain injury
TD-OCT: time domain-OCT
TSCW: thinned-skull cortical window
WDM: wavelength division multiplexer

Chapter 1. Background

1.1. Optical coherence tomography

Optical coherence tomography (OCT) is an optical imaging modality capable of producing cross-sectional images of biological tissue that was first demonstrated in 1991 by Huang *et al.* for imaging the retina *in vitro* [1]. Since then OCT has become an important tool for biomedical imaging in numerous fields because of its ability to perform "optical biopsy" on intact biological samples in a depth-resolved manner [2–4]. The micrometer resolution of OCT combined with its ability to achieve two-dimensional (2D) and 3D imaging of biological tissue in real time using only the inherent optical contrast of the sample allows OCT to form histology-like images without the need to excise and stain the sample, making it an ideal technique for *in vivo* imaging. OCT can achieve a resolution of 1-10μm and imaging depths of 1-3 mm in biological samples. This combination of resolution and penetration depth allows OCT to fill a void left by other conventional imaging techniques such as confocal microscopy, which has better resolution but much smaller penetration depth, and ultrasound, which is able to image deeper with lower resolution (Figure 1.1). With this unique combination of resolution and imaging depth, OCT has found widespread clinical and research applications in fields including ophthalmology [3,5–7], cardiology [8–10], dermatology [11,12] and neuroscience [13].

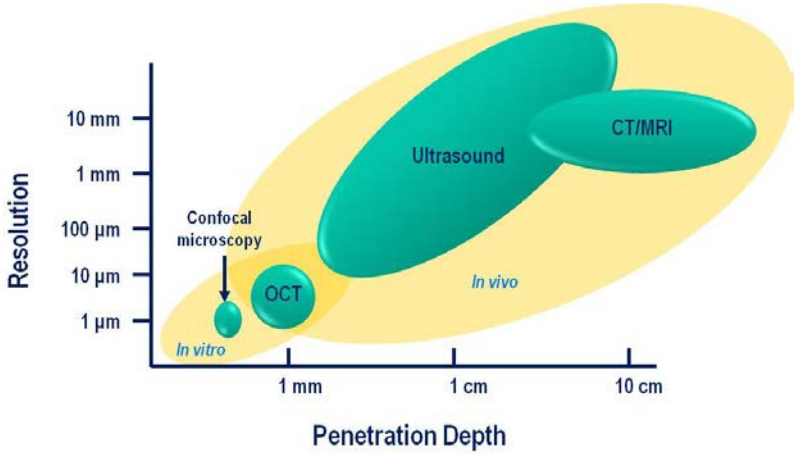

Figure 1.1 Comparison of image depth and resolution for OCT and other conventional imaging technologies.

1.1.1. Principle of OCT

The basic principle of OCT is analogous to ultrasound. Ultrasonic imaging creates depth-resolved structural images of a sample by sending a sound pulse into the sample and measuring the amplitude and time delay of that sound wave reflecting back from the sample and returning to the detector. Shallow reflectors within the sample yield shorter delay times while deeper reflectors produce longer delays. OCT achieves depth-resolved imaging in the same manner using light pulses rather than sound pulses. However, since light travels much faster than sound ($v_{light} = 2.998 \times 10^8 m/s$ compared to $v_{sound} = 343\ m/s$) the time delay cannot be directly measured but rather must be determined using low coherence interferometry.

Low coherence interferometry is typically implemented with a Michelson interferometer setup and a low coherence light source (Figure 1.2). Light from the source is split between sample and reference arms. Each arm reflects part of the light back along the incident path. The reflected light from each arm then recombines and

travels toward the detector. The interference formed by recombining the light from each arm encodes the depth-resolved reflectance information of the sample. By utilizing a low coherence light source, constructive interference is only observed when the pathlength mismatch between the sample and reference arms is within the coherence length of the light source, allowing for precise depth-resolved imaging. In contrast, if a highly coherent light source is used, the interference pattern would be observed over a number of pathlength differences between the two arms.

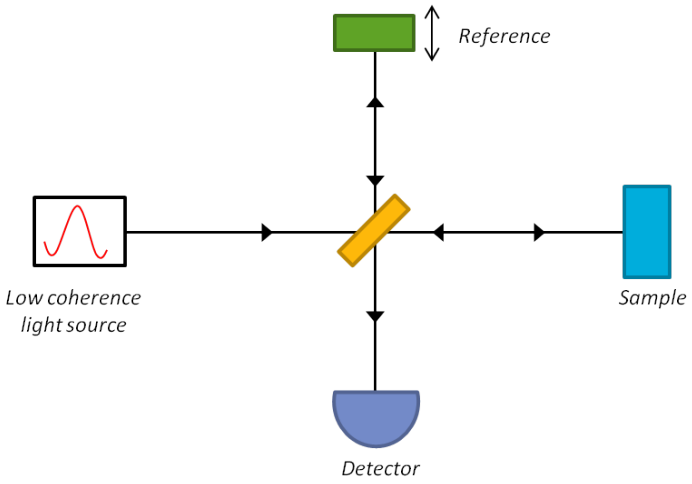

Figure 1.2 Low coherence interferometry setup using a Michelson interferometer.

In time-domain (first-generation) OCT, the intensity of the interferogram is detected by a single-channel photoreceiver [1]. Scanning the reference arm over a given length allows the sample reflectivity to be probed as a function of depth. The measured intensity then provides a depth-profile, also known as an A-line, which describes the sample reflectivity as a function of depth. A 2D cross-sectional image is formed by acquiring sequential A-lines and is achieved by scanning the optical beam across the

sample in a given direction and arranging each A-line side by side to form a 2D matrix. The intensity values in this matrix are then represented by a color as designated by the chosen colormap. Similarly taking consecutive 2D scans at different lateral positions builds a 3D representation of the sample (Figure 1.3).

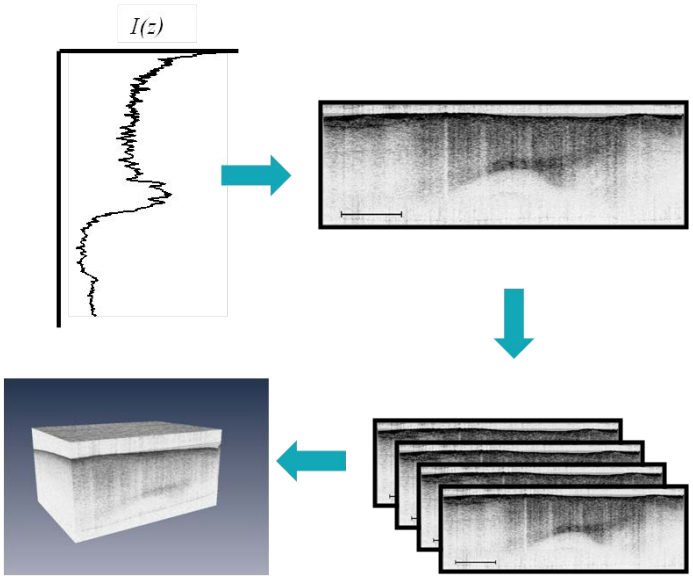

Figure 1.3 A depth profile (top left) represents the intensity as a function of depth. Scanning the optical beam across the sample creates a series of depth profiles that can be represented as a cross-sectional image. Scanning a series of 2D images creates a 3D volume. Images shown were taken of an *in vivo* murine brain over the right cerebral cortex in a sagittal orientation.

1.2. Spectral-domain OCT

Spectral domain OCT (SD-OCT) is the second-generation of OCT technology and was first demonstrated in 1995 [14], but the advantages of spectral domain detection were not recognized until 2003 [15–17]. While SD-OCT systems are very similar to that of TD-OCT, there are two important differences: (1) the reference arm remains stationary and (2) the interfered light in the detection arm is dispersed through a grating and detected in

a spectrally resolved manner on a line scan camera. A typical SD-OCT system implemented using fiber optics is shown in Figure 1.4. The light is sent into a circulator and then to an optical splitter to split the light between the reference arm and sample arm. The reflected light from each arm travels back through the same optical fiber and through the splitter. The interfered light then is redirected by the circulator to the detection arm where the light is collimated, dispersed by a grating, and focused onto a line scan camera. Raster scanning of the optical beam to achieve 2D and 3D imaging is performed by galvanometer mounted mirrors in the sample arm that are controlled by the image acquisition program.

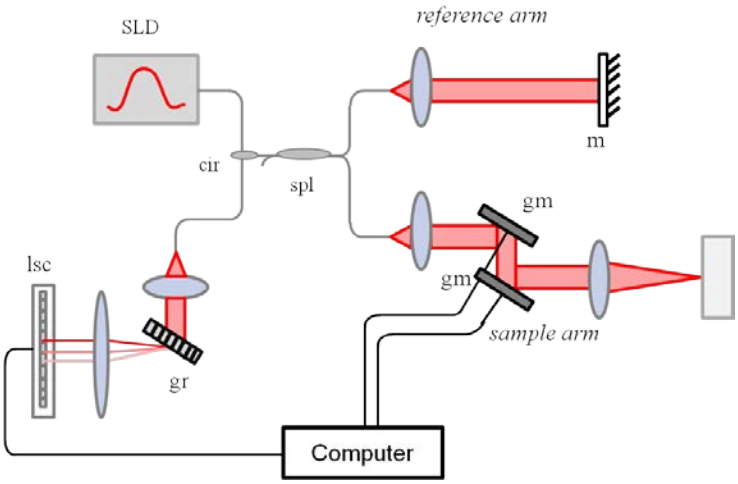

Figure 1.4. Schematic of SD-OCT system. SLD: superluminescent diode, cir: circulator, spl: splitter, m: mirror, gm: galvanometer mounted mirror, gr: grating, lsc: line scan camera.

The intensity, I_d, at the detector can be expressed as [18],

$$I_d(k,\omega) = \frac{\rho}{2}\langle E_r + E_s\rangle^2 \qquad \textit{(Eq. 1-1)}$$

where ρ represents the detector sensitivity, and E_r and E_s represent the electric field from the reference arm and sample arm, respectively. Assuming a polychromatic light source, the incident field can be written as $E_i = s(k,\omega)e^{i(kz-\omega t)}$, where *s(k,ω)* represents the amplitude as a function of wavenumber, *k*, and angular frequency, *ω*. Hence, when this light is split between the sample arm and reference arm (in this case we will assume equal splitting of power) the reference and sample fields can be written in terms of the incident field as,

$$E_r = \frac{s(k,\omega)}{\sqrt{2}}\sqrt{a_r}exp[i(2kz_r - \omega t)] \qquad \textit{(Eq. 1-2)}$$

$$E_s = \frac{s(k,\omega)}{\sqrt{2}}\sqrt{a_s}exp[i(2kz_s - \omega t)] \qquad \textit{(Eq. 1-3)}$$

assuming a single reflector in each arm, with reflectance of a_r and a_s, at an optical pathlength of z_r and z_s respectively. Note the factor of two in the exponential argument accounts for the round trip pathlength the light experiences traveling to the reflector and back. Imaging of biological samples is better described by a series of reflectors at various depths within the sample, rather than a single reflector, the sum of which make up the total signal detected. Therefore, a more realistic electric field expression for the sample arm can be written as,

$$E_s = \frac{s(k,\omega)}{\sqrt{2}}\sum_{n=1}^{N}\sqrt{a_{s_n}}exp\left[i(2kz_{s_n} - \omega t)\right] \qquad \textit{(Eq. 1-4)}$$

Upon substitution of *Eq. 1-2* and *Eq. 1-4* into *Eq. 1-1* the intensity at the detector can be expressed as [18,19],

$$I_d(k) = \frac{\rho}{4} s(k)^2 \Big[a_r + \sum_{n=1}^{N} 2\sqrt{a_r a_s}\ cos\big(2k(z_r - z_{s_n})\big) + \sum_{n=1}^{N}\sum_{m=1}^{N} \sqrt{a_{s_n} a_{s_m}} \big(exp\big[i2k(z_r - z_{s_n})\big]\ exp\big[-i2k(z_r - z_{s_m})\big]\big)\Big] \quad \textit{(Eq. 1-5)}$$

The final expression consists of three terms. The first term is simply an offset. The second term is the interferometric term and provides the depth information of the sample where the amplitude of the backscattering is proportional to the a_s factor and the frequency of the cosine encodes the axial position. The third term contains autocorrelation information of the interference between all the scatterers within the sample and is only observed near $z = 0$ [19,20]. The intensity of the sample as a function of depth is retrieved from this interference signal by performing a Fourier transform from the k (wavenumber) domain to the z (spatial) domain [14,19,21].

$$\begin{aligned} FT^{-1}\{I_d(k)\} &= I(\Delta z) \\ &= FT^{-1}\left\{\frac{\rho}{4}\ s(k)^2 a_r\right\} + \\ &\quad FT^{-1}\left\{\frac{\rho}{2} s(k)^2 \sum_{n=1}^{N} 2\sqrt{a_r a_s}\ cos\big(2k(z_r - z_{s_n})\big)\right\} + \\ &\quad FT^{-1}\left\{\frac{\rho}{4} s(k)^2 \sum_{n=1}^{N}\sum_{m=1}^{N} \sqrt{a_{s_n} a_{s_m}} \big(exp\big[i2k(z_r - z_{s_n})\big]\ exp\big[-i2k(z_r - z_{s_m})\big]\big)\right\} \end{aligned} \quad \textit{(Eq. 1-6)}$$

$$\begin{aligned} I(\Delta z) &= \frac{\rho}{8}\big[\gamma(z)\ \big(\mathrm{a_r} + \mathrm{a_{s_1}} + \mathrm{a_{s_2}} + \cdots\big)\big] + \\ &\quad \frac{\rho}{4}\ \big[\gamma(z) \otimes \sum_{n=1}^{N} \sqrt{\mathrm{a_r a_s}}\ \delta\big(\mathrm{z} \pm 2(\mathrm{z_r} - \mathrm{z_{s_n}})\big)\big] + \\ &\quad \frac{\rho}{8}\big[\gamma(z) \otimes \sum_{n \neq m=1}^{N} \sqrt{\mathrm{a_{s_n} a_{s_m}}}\ \delta(\mathrm{z} \pm 2(\mathrm{z_{s_n}} - \mathrm{z_{s_m}}))\big] \end{aligned} \quad \textit{(Eq. 1-7)}$$

where $\gamma(z)$ represents the Fourier transform of the power spectral dependence term $s(k,\omega)^2$ and $\otimes$ denotes convolution.

The theoretical axial resolution of a SD-OCT system can be determined from *Eq. 1-7*. Assuming the light source has a Gaussian shape (i.e. $|s(k)|^2 = \frac{1}{\Delta k\sqrt{\pi}} \exp\left[-i\left(\frac{k-k_o}{\Delta k}\right)^2\right]$), for a single reflector in the sample arm (*N=1)* the interferometric term in Eq. 1-5 will contain a single frequency and thus a single delta function convolved with the Gaussian will be obtained from the interference term of the final intensity depth profile expression (*Eq. 1-7*). This directly dictates the full width half max (FWHM) axial resolution, δz, of the OCT system:

$$\delta z = \frac{2\,ln2}{\pi}\frac{\lambda_o^2}{\Delta\lambda} \qquad \textit{(Eq. 1-8)}$$

As is clear from Eq. 1-5, imaging a complex biological sample rather than a single reflector produces a spectrum that is simultaneously modulated by a multitude of frequencies of varying amplitudes. A Fourier transform of this signal produces a complete depth profile from data obtained during a single camera acquisition. Hence, detection in the spectral-domain removes the need to scan the reference arm and make multiple measurements during acquisition of each depth profile. This not only increases the speed at which OCT images can be taken but also increases the signal to noise ratio (SNR) of the system compared to conventional TD-OCT [15–17].

1.2.1. Wavelength mapping to *k*-space

As described in the previous section, the depth resolved information of the sample is obtained through a Fourier transform of the spectral intensity function in the *k* domain to the *z* domain, which requires the data to be evenly sampled in *k*-space. The correct wavelength assignment for each pixel on the camera can be achieved through calibration of the system by starting with an approximate wavelength assignment generated from the grating equation and then iteratively applying corrections [22]. Each wavelength can then be converted to a wavenumber ($k = 2\pi/\lambda$) and then resampled at regular intervals in *k*-space by using interpolation, prior to the Fourier transform.

1.2.2. Spectrometer design considerations for imaging range and sensitivity fall-off

The design of the spectrometer within an SD-OCT system has far reaching effects on the final image quality. It determines the maximum imaging range and the amount of sensitivity fall-off and can also diminish the axial resolution if not carefully designed. The main components of a spectrometer include the grating, focusing lens and camera used to measure the spectrum (Figure 1.5)

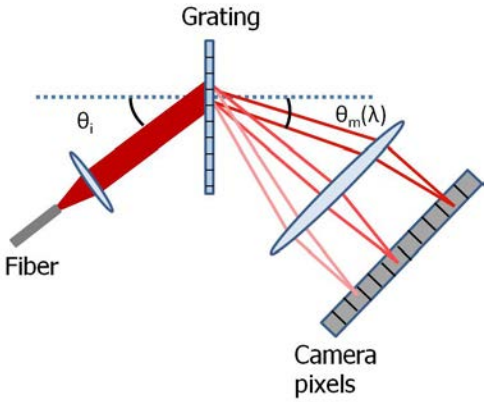

Figure 1.5 Basic spectrometer setup for SD-OCT system.

The imaging range defines the maximum imaging depth that can be achieved by the OCT system. For SD-OCT systems, the axial position of the reflector in the sample arm is directly related to the frequency of the modulation on the measured spectrum. Low frequency modulations correspond to shallow reflectors while high frequency modulations are produced by deep reflectors. Therefore, the maximum depth at which a reflection can be measured is limited by the maximum frequency that can be measured on the line scan camera. This occurs when the sampling rate is equal to twice the maximum frequency (known as the Nyquist criterion). The spectrum is sampled with a wavelength resolution or wavelength bin size, $\Delta\Lambda$, on the spectrometer. When a continuous signal is sampled discretely, the wavelength resolution is related to the spatial resolution (pixel size), Δz, by [19],

$$\Delta z = \frac{\lambda^2}{2\,N\,\Delta\Lambda} \qquad \textit{(Eq. 1-9)}$$

Therefore, the wavelength spacing on the spectrometer should be chosen such that the pixel size in the spatial domain is smaller than the theoretical axial resolution, as

determined by the light source (Eq. 1-8). Otherwise, the axial resolution of the system will be reduced. Choosing a pixel size of one half of the axial resolution will allow for two reflections separated by δz to be resolved. Substituting $\delta z/2$ into Eq. 1-9 determines the ideal wavelength spacing to maximize the imaging range while preserving the axial resolution:

$$\Delta\Lambda = \frac{\pi\,\Delta\lambda}{2\,ln2\,N} \qquad \textit{(Eq. 1-10)}$$

With the wavelength spacing given by the above equation, the maximum imaging range is [19,20,23]:

$$\Delta z_{max} = \frac{\Delta z}{2}\,\frac{N}{2} = \frac{ln2\,\lambda_0^2 N}{2\pi\,\Delta\lambda} \qquad \textit{(Eq. 1-11)}$$

Note the factor of two in the denominator is included because of the complex conjugate symmetry around $z=0$ following the Fourier transform.

In addition to design consideration for imaging range, the spectrometer specifications affect the sensitivity fall off inherent to all SD-OCT images [21,24]. Reflections of the same magnitude positioned deeper in the imaging range register a lower SNR compared to the same reflector positioned at a shorter pathlength difference after processing the A-line (Figure 1.6).

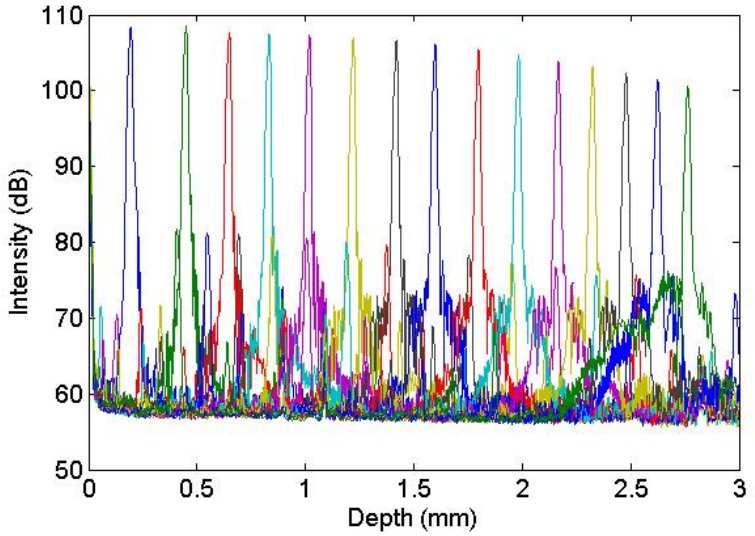

Figure 1.6 Reflections off of a mirror positioned at various heights show the sensitivity fall off as a function of depth from SD-OCT system centered at 1300nm.

The decrease in system sensitivity as a function of depth is due to "cross-talk" between pixels on the line scan camera caused by imperfect focusing of the final lens in the spectrometer and also the finite size of each pixel [20,25]. Light entering the spectrometer is first collimated and then passes through a grating which disperses the light, sending different wavelengths out at different angles. The focusing lens focuses each wavelength to a pixel on the camera. The focus spot size or point spread function (PSF) of each wavelength can be reasonably well described by a 2D Gaussian. While the Gaussian PSF is centered on a single pixel, the tails of the Gaussian extend over neighboring pixels and contribute to the power read by each of those neighboring pixels. This "cross-talk" becomes increasingly significant as the modulation frequency increases. As depicted in Figure 1.7A, at low frequency modulations, the cross-talk between neighboring pixels does not significantly change the overall power read by each pixel

since the tails of the Gaussian PSF on each pixel have similar overlap from one pixel to the next. However, for higher frequency modulation, the cross-talk between neighboring pixels varies greatly and works to reduce the measured amplitude (Figure 1.7B). Additionally, because each pixel on the camera has a finite size and therefore cannot collect all of light contained in each PSF, this also contributes to decreased sensitivity as a function of depth.

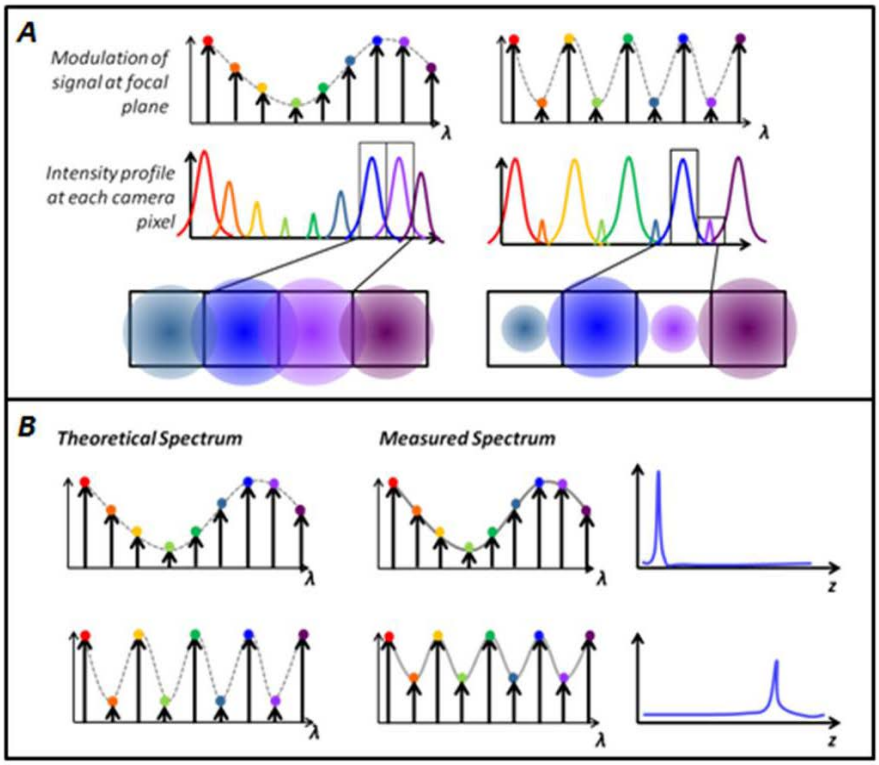

Figure 1.7 (A) The PSFs shown on a per pixel basis for (left) low frequency modulation (right) and high frequency modulation illustrate the varying degrees of pixel cross-talk. (B) Schematic of the decreased amplitude measured due to pixel cross talk and its effect on the resulting amplitude in the intensity depth profile.

By assuming a Gaussian PSF for the focused spectrum and a square pixel shape on over which the intensity is integrated by the camera, the sensitivity drop off as a function of depth can be described by [21],

$$R(z) = \frac{sin^2(\pi z/2z_{max})}{(\pi z/2z_{max})^2} exp\left[-\frac{\pi^2\omega^2}{8\,ln2}\left(\frac{z}{z_{max}}\right)^2\right] \qquad \textit{(Eq. 1-12)}$$

where ω represents the ratio of the spectral resolution to the wavelength sampling interval.

1.3. Functional extensions of OCT

In addition to depth resolved intensity (reflectance) information that identifies structural information in the sample, OCT can provide other information about the sample including location and magnitude of fluid flow as well as the birefringence of the sample. Flow is identified by Doppler OCT, a post-processing technique applied to the same data acquired during normal OCT acquisition that compares the phase of adjacent A-lines to identify the Doppler shift encoded when light reflects off of a moving particle [26–28]. Using this technique in combination with conventional OCT enables simultaneous visualization of tissue structure and blood flow at high resolution (Figure 1.8 A,B [29]).

Measuring the birefringence of a sample offers another mode of contrast. A birefringent material is one in which the refractive index depends on the polarization state and is typically exhibited by biological material that is highly organized, such as fibrous muscle or tendon and the myelin sheath that surrounds nerve axons. In order to measure the birefringence of a sample with SD-OCT, additional components must be included in the system. The incident light must be sent through a polarization modulator that alternates the light between two orthogonal polarization states between adjacent A-lines. The detection arm must also be modified to include a polarizing beam splitter and a

second camera to detect the orthogonal polarization states separately. With this information, polarization sensitive OCT (PS-OCT) can calculate the phase retardation as a function of depth between the two orthogonal polarization states to provide a measure of the sample's birefringence [30–32]. In PS-OCT images, the phase retardation value ranges between *0,* (represented in black) and *,π* (represented in white), causing highly birefringent materials to exhibit a banding pattern, going through multiple black-to-white transitions (Figure 1.8 C [29]).

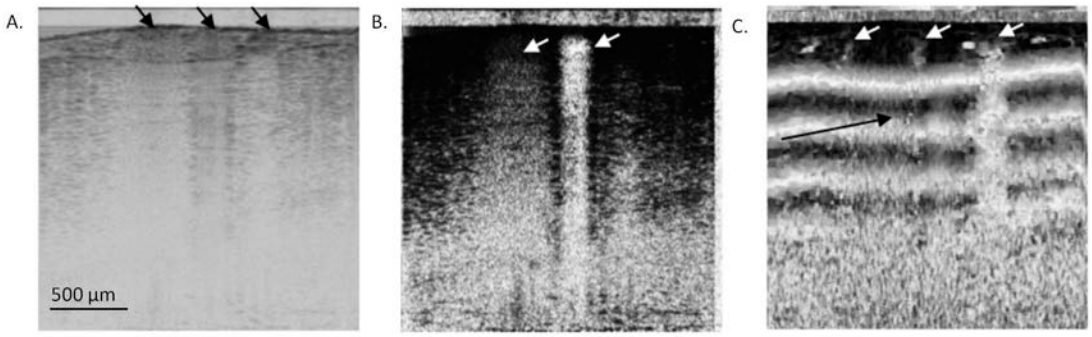

Figure 1.8 OCT image of mouse hind leg muscle with femoral artery, vein and nerve indicated by arrows in the (A) intensity image, (B) Doppler OCT phase variance image and (C) accumulated phase retardation image [29].

1.4. Current OCT applications to neuroimaging

In recent years OCT has found increasing application in the areas of neuroscience and neuroimaging. Structural imaging by OCT has been used in developmental biology to further the understanding of the developing central nervous system and brain development *in vivo* in Xenopus, Zebrafish and mouse models [33–35]. Additionally the feasibility of using OCT for identifying various brain structures and markers in adult mammalian animal models has been explored in various mouse and rat models [36–39].

Such structural imaging is highly advantageous over standard microscopy techniques and histomorphological analysis for studying tissue structure and microstructure because no exogenous contrast agents are needed. Additionally, repeated imaging of the same *in vivo* sample can be performed, which reduces the need to sacrifice the animals and allows for the same sample to be probed at multiple time points. Optical detection of neuronal activity using OCT has also found increasing interest in recent years. Scattering changes correlated with neuronal activity as well as analysis of hemodynamic changes from *in vivo* and *in vitro* experiments have been reported [40–43].

1.5. Cerebral edema

The focus of this dissertation is the development and application of OCT for cerebral edema detection. Cerebral edema is a condition characterized by a net increase in brain water content. It is caused by traumatic injury, tumor and ischemia and leads to brain swelling and raised intracranial pressure (ICP). The secondary damage caused by brain swelling greatly increases the morbidity and mortality associated with these conditions. Nearly 1.7 million people experience traumatic brain injury (TBI) each year in the United States and it is considered a contributing factor in one-third of all injury-related deaths [44]. Early and precise detection and monitoring of cerebral edema is crucial for understanding edema development and dynamics, evaluating the effectiveness of new treatment strategies as well as guiding clinical treatment decisions.

Cerebral edema can be classified as either vasogenic or cytotoxic edema [45]. Vasogenic edema occurs due to increased permeability of the blood brain barrier (BBB),

allowing for a large influx of fluid into the surrounding tissue. Cytotoxic edema refers to an increase in intracellular fluid, characterized by cell swelling. Cells swell due to changes in intracellular and extracellular ion concentrations resulting from failure of active transport mechanisms. The intracellular volume increases at the expense of the extracellular space (ECS) and therefore, cytotoxic edema does not cause a rise in ICP by itself. However, the shift in ECS ion concentrations increases the driving force for ions and water crossing the BBB which causes a net increase in volume and ICP [46]. Cellular swelling also leads to cellular dysfunction through alterations to intracellular ion and metabolite concentrations [47].

1.5.1. Detection and monitoring of cerebral edema

Cerebral edema is most commonly assessed indirectly using intracranially placed pressure transducers. This method allows for continuous monitoring and is used to make therapeutic decisions about hyperosmolar treatment and surgical decompression. However, there are several drawbacks to this method. First, due to the nonlinear compliance (pressure-volume relationship) of brain tissue, ICP cannot provide an accurate measure of early edema development [48–50]. The volume of the brain increases at the onset of edema due to the increase in water content, but this increase is offset by a compensatory decrease in other components, such as blood or cerebral spinal fluid volume (Monro-Kellie doctrine) [48]. ICP increases only after a significant amount of water has collected in the brain and the compensatory volume reserve is exhausted. This makes detection of cerebral edema especially difficult in the early stages when

treatment could be administered to prevent secondary injuries. Secondly, the noise within the ICP measurement increases as ICP increases, leading to less precise measurements. Lastly, a number of physiological parameters, such as head position, blood pressure and respiration affect ICP [49,51] and this circumstantial variability makes it difficult to define a precise ICP value for edema detection. Consequently, an ICP threshold erring on the large side at about 20 mmHg has been classified as abnormal (normal ICP in a healthy adult range 7-15 mmHg) [49]. This threshold is typically used to trigger clinical intervention, by which time significant edema has developed. It should also be noted that CT or MRI serial scans may also be used to diagnose edema. However, these methods require patient movement, significant time and labor resources, and they do not allow for continuous, real-time monitoring.

Optical methods show promise for improved detection of cerebral edema compared to the current state of the art. In particular, an increase in light transmittance was observed from in vitro brain slices after perfusion with hypotonic solution to induce cerebral edema [52]. Also, previous work done in Dr. Devin Binder's laboratory demonstrated a decrease in reflectance of near-infrared light from brain tissue of an *in vivo* cytotoxic cerebral edema mouse model and this intensity decrease occurred a significant amount of time before the ICP detection of edema was achieved [53]. During cerebral edema, the water flux into the brain increases and causes cell swelling [54] and this change in tissue composition alters the light scattering pattern of the tissue. The primary advantage of optical detection is the direct relationship between tissue

composition and light scattering, in contrast to the indirect, complex relationship between ICP and brain volume.

1.6. Conclusion

While the previous studies provide proof-of-principle for optical detection of cerebral edema, their usefulness is limited by the micrometer level light penetration depth in tissue, the lack of spatially-resolved information and the invasive nature of the intracranially placed fiber optic probe. The goal of this work is to develop a minimally invasive, spatially resolved early optical detection method for cerebral edema using OCT. The unique combination of resolution and imaging depth offered by OCT is ideal for characterizing the spatiotemporal progression of cerebral edema in a small animal model.

Chapter 2. Detection of global cytotoxic cerebral edema *in vivo* using OCT

2.1. Introduction

Cerebral edema, an increase in brain water content, occurs due to a variety of conditions and injuries and can be classified as either cytotoxic or vasogenic edema. Cytotoxic cerebral edema occurs when cells in the brain swell with excess water while the BBB remains uninterrupted. In contrast, vasogenic edema occurs due to increased permeability of the BBB and leads to excess water accumulation in the extracellular space. A number of different animal models have been developed to study cerebral edema development and the effects of possible treatments. These models range from simplistic models with well characterized results, such as water intoxication, to more clinically relevant models of stroke or blunt force trauma that exhibit more varied results. In order to first detect optical changes measured with OCT that are associated with cerebral edema onset and progression, we began with a water intoxication mouse model, which causes cytotoxic cerebral edema globally throughout the brain. This model has been well characterized and proven to increase in brain water content. In this study, we used OCT to analyze how the light backscattered from the brain changes during cerebral edema progression in a water intoxication mouse model.

2.2. Experimental methods

This section describes the use of OCT for *in vivo* murine brain imaging and as well as the methods used during the water intoxication experiments. It begins with a description of the thinned skull cortical window (TSCW) used to increase imaging depth without removing the skull. Then, registration of OCT images with histology for brain structure identification is described. Lastly, the details of the water intoxication animal model, experimental imaging parameters and data analysis used to for the characterizing the optical changes that occurred during edema progression are explained.

2.2.1. Preparation of thinned skull cortical window

Female CD1 wild-type mice, 6-14 weeks old, were anesthetized with an intraperitoneal (IP) injection of ketamine and xylazine (10 mg/kg xylazine, 80 mg/kg ketamine) and prepared with a TSCW, approximately 4x4 mm^2 wide, centered over the right cerebral cortex, by using a round carbide bur to slowly thin the bone to approximately 55 μm [55]. The thinned skull allowed for increased light penetration depth while preserving the natural physiological conditions of the brain (Figure 2.1) [55]. The mouse can then be secured in a stereotactic frame for stable OCT imaging over a select region of interest within the cortical window.

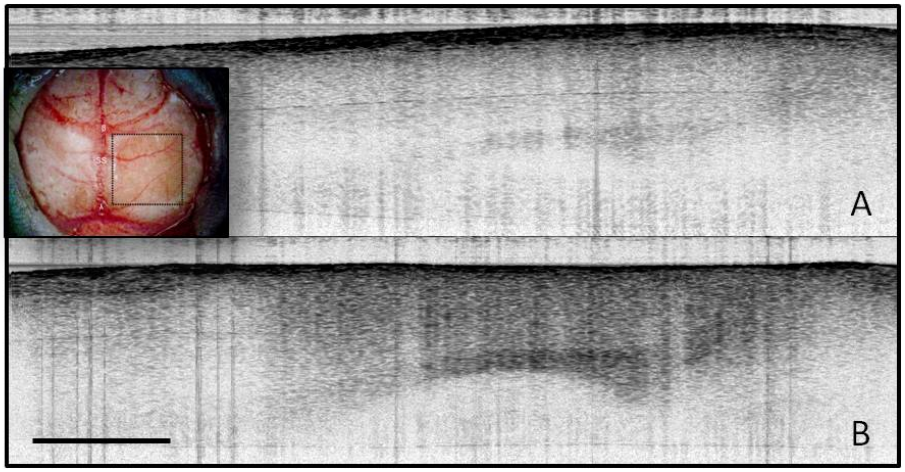

Figure 2.1 (Inset) Thinned skull cortical window over right cerebral cortex, outlined by dotted square box, (A) OCT image *in vivo* mouse brain in sagittal orientation through normal skull thickness and (B) thinned skull cortical window, providing greater imaging depth. Scale bar = 1 mm. [55]

2.2.2. Identification of brain structures in OCT images

Separate OCT imaging of an *in vivo* murine brain was conducted to register the OCT images with histology and identify the brain structures visible in the OCT image taken through the TSCW. OCT images were collected in a sagittal plane approximately 1 mm lateral from midline. The imaging plane was identified by marking the skull with two small ink marks to indicate the boundaries of the imaging plane. The mouse was then removed from the imaging system and two burr holes were made at these sites, approximately 1 mm caudal to the coronal suture and 1 mm rostral to the lambdoid suture. Five 50 nL India ink injections (250 nL total volume) were given at each burr hole site using a nano injector at a depth of 1.9 mm. The microinjection pipet was slightly retracted after each successive injection to ensure an ink tract was made. OCT

images were acquired once more in this plane in order to register the India ink markers with the same markers on histology.

After OCT data acquisition was complete, the mouse was deeply anesthetized and transcardially perfused with 5 mL of phosphate buffered saline (PBS) followed by 5 mL of 10% buffered formalin. The brain was then dissected and cryoprotected in 30% sucrose in PBS for at least 48 hours. It was cryosectioned into 50 μm thick slices and mounted on glass slides for Nissl staining. The resulting histology was imaged using a Nikon stereoscopic microscope with a 10X magnification.

Brain structure identification was achieved by registering the images with histology (Figure 2.2). The India ink tracts visible under the burr holes in the OCT images (Figure 2.2 A) frame light and dark contrast areas of the brain. These tracts were largely preserved throughout histological processing, although some of the ink on the brain surface was removed during the dissection and cryosection procedures (Figure 2.2 B). Comparison of the histology to the OCT image revealed the lower intensity region directly underneath the skull is the cerebral cortex (gray matter) and the higher intensity region below the cortex is the corpus callosum (white matter). This was also confirmed by overlaying the histology with the control OCT image taken before the India ink was injected (Figure 2.2 C). The corpus callosum in the OCT image aligned well with the histology.

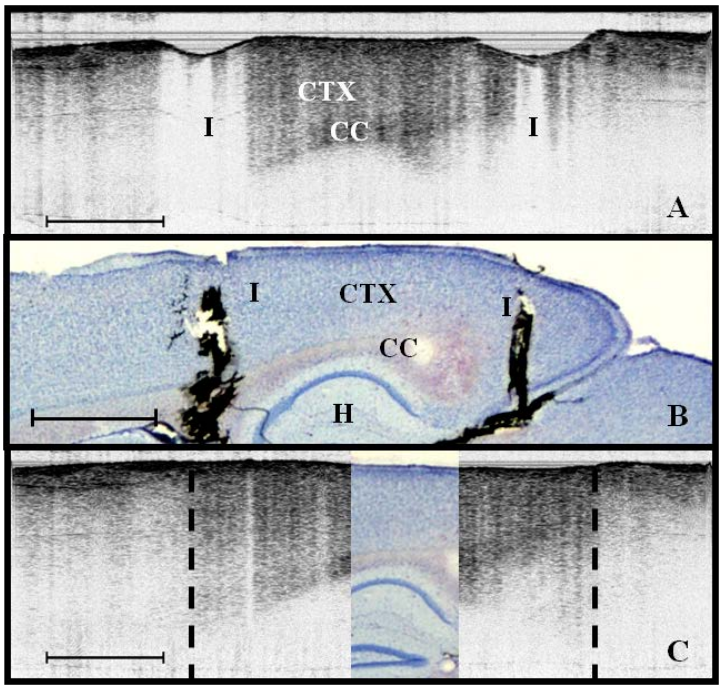

Figure 2.2 (A) OCT image of murine brain in sagittal orientation with India ink markers made through two burr holes in the skull, (B) corresponding histology image showing the same India ink markers and (C) histology overlaid on OCT image identifying the cerebral cortex and corpus callosum. Scale bar = 0.5 mm

2.2.3. Water intoxication animal model

An acute water intoxication model of cytotoxic cerebral edema, in which water is driven from the vascular system into the brain by an osmotic gradient, was used [56,57]. Twenty minutes of baseline OCT imaging was performed after which an IP injection of water was given (dosage 40% of the animal's body weight). OCT imaging continued for 60 minutes. One OCT volume was collected every 3 minutes and spanned a volume of 4 x 4 x 2 mm^3. Three water intoxication experiments and 3 control experiments (including thin-skull preparation, without IP injection) were performed. All experimental

procedures and protocols were approved by the University of California Riverside Institutional Animal Care and Use Committee (protocol 2010-0018).

2.2.4. Brain water content analysis

Presence of cerebral edema was verified by analyzing brain water content (BWC) via the wet-dry method. After OCT data collection was completed animals were sacrificed and the brains were dissected out post-mortem and cut into four pieces (right-left cerebral hemispheres, right-left cerebellum). Brains were weighed to obtain wet weight and dried for 48h to determine dry weight. Percent water content was calculated with the following formula: *BWC = [(wet weight - dry weight)/wet weight] x 100.*

2.2.5. OCT image acquisition

A spectral-domain OCT system centered at 1300 nm was used to image the *in vivo* mouse brain (shown previously in Figure 1.4). The light source consisted of two superluminescent diodes (SLD) with a combined center wavelength of 1298 nm and a 120 nm full-width half-maximum bandwidth (FWHM). The source light was sent through a fiber optic circulator and an 80/20 splitter, which divided the light between the sample arm and reference arm. The light that reflected from a mirror in the reference arm and from the brain tissue in the sample arm was then recombined at the splitter, dispersed by a grating and detected on the line scan camera. Each spectrum acquired by the camera contained depth information from a single x-y location in the sample (A-line). Three dimensional imaging was achieved by raster scanning the optical beam across the sample

using two galvanometer mounted mirrors. The system has an axial imaging range of approximately 2 mm in biological tissue, an axial resolution of 8 μm, and a lateral resolution of 20 μm.

Each image contained 2048 A-lines, acquired at a rate of 15 kHz, and 250 images were used to render a single volume. Real-time visualization of the sample was achieved using in-house developed software, which utilized a graphics processing unit (GPU) to process and display the OCT structure and blood flow images in real time [58]. The real-time display of OCT images allowed for structural markers within the imaging location to be rapidly identified and ensured that the same region of the brain was consistently imaged during and across all experiments. Depth-resolved structural information was retrieved from each A-line by applying a Fourier transform to the spectrum collected on the camera after linearly remapping to *k*-space, as described in Chapter 1. The images were displayed on an inverse log scale.

Images of the cerebral vascular network were generated by utilizing the phase information contained in the OCT signal, a method known as Doppler OCT (DOCT) [27,59,60]. This technique enables high resolution imaging of motion within the sample by calculating the Doppler frequency shift caused from reflection off of a moving sample. The depth resolved phase difference between consecutive A-lines was determined and this phase difference is directly proportional to the axial component of the velocity of the scattering particle. Static tissue introduces minimal phase shifts and is represented by low intensity in DOCT images while blood flow induces a large phase difference, represented by high intensity.

2.2.6. Analysis of attenuation coefficient and cerebral blood flow

In this study, the change in the tissue's average attenuation coefficient was used to quantify the effects of cerebral edema in the cerebral cortex. The attenuation coefficient is an optical property of a material that describes how strongly the sample scatters and absorbs light. The intensity decay in depth can be described by the Beer-Lambert law:

$$\frac{I(z)}{I_o} = e^{\int_0^z \mu(z)dz} \qquad \textit{(Eq. 2-1)}$$

where I_o is the incident intensity, $I(z)$ is the intensity at depth z and $\mu(z)$ is the attenuation coefficient of the sample as a function of z. The attenuation coefficient was determined on a pixel-by-pixel basis using a recently developed model for depth-resolved attenuation coefficient determination in OCT data [61]. This method makes it possible to create an attenuation image, in which contrast is indicated by the local attenuation coefficient, from an OCT intensity image with known pixel size. The tissue was assumed to have an index of refraction of 1.4.

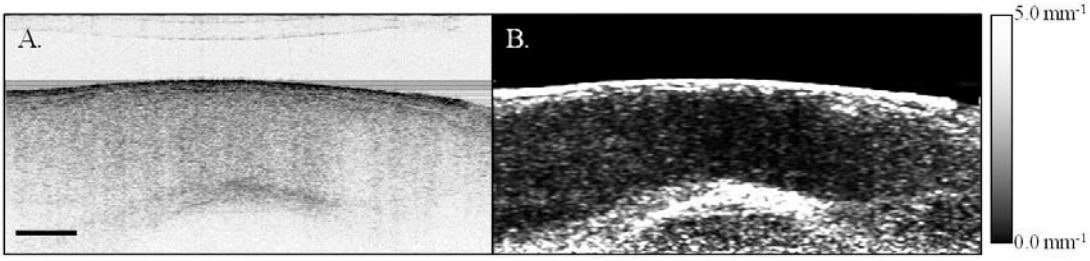

Figure 2.3. (Left) OCT intensity image of in vivo mouse brain in a sagittal orientation and (right) the corresponding attenuation image. Scale bar = 0.5 mm

The average attenuation coefficient of the cortex was determined over time as edema progressed in the animal model. All pixels contained in the regions of interest

(ROI) and within 0.6 mm of the surface (gray matter region) were included in the average calculation. The average attenuation coefficient during baseline was determined from all data acquired during the first twenty minutes and the percent change in the average attenuation coefficient was calculated at all points in subsequent volumes.

Cerebral blood flow was analyzed by calculating the percent change in flow density using the DOCT image information. A threshold was set to distinguish pixels that represent flow from background pixels in the DOCT data, within the same ROIs that were used for attenuation analysis. The total DOCT intensity was calculated as the sum of all intensities in pixels identified as flow regions and divided by the number of pixels in the ROI to determine the flow density. The percent change in flow density was then calculated for each time point in order to determine how the cerebral blood flow was changing over time. Maximum intensity projection (MIP) images of the cerebral blood flow were displayed in an *en face* orientation and filtered using a Gabor filter [62].

2.3. Results of water intoxication model

2.3.1. Attenuation changes from *in vivo* cerebral edema model

The percent change in attenuation coefficient was determined from the OCT attenuation data within a 3x3 mm^2 ROI over the cerebral cortex. The areas close to the cortical window boundaries were excluded from the calculation because of uneven bone thickness in these regions. The average value of the attenuation coefficient in the

cerebral cortex remained steady during baseline and then decreased soon after the IP injection was administered at twenty minutes (Figure 2.4). The decrease continued approximately linearly in time as cerebral edema progressed. A maximum decrease of 8% was observed by the end of the experiment (at which time standard error of the mean was 1.93). Over the same amount of time, the average attenuation coefficient from the control experiments remained relatively constant (Figure 2.4). The BWC measurements confirmed that the cerebral edema group exhibited higher brain water content compared to the control group (Figure 2.5).

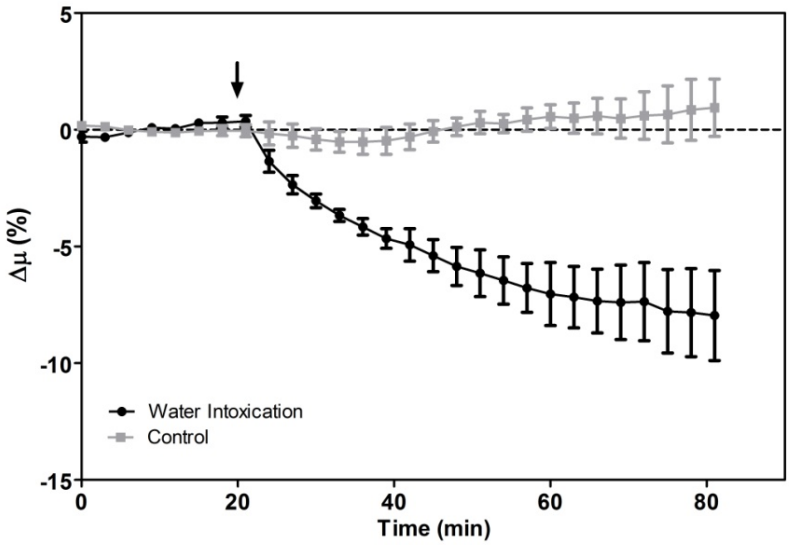

Figure 2.4. Percent change of average attenuation coefficient in the cerebral cortex over time from *in vivo* water intoxication mouse model. Arrow indicates IP water injection for water intoxication group. Error bars represent standard error for *n=3.*

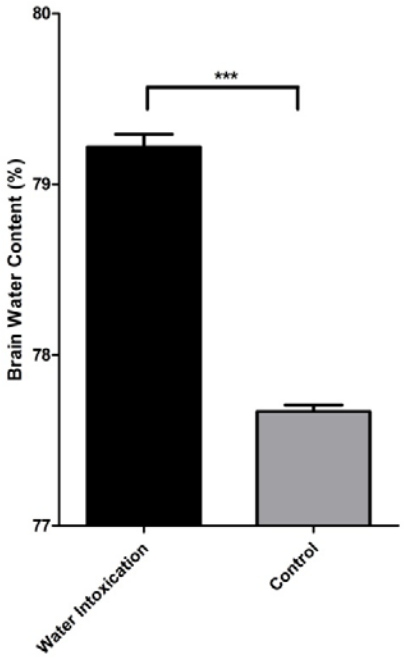

Figure 2.5. BWC measurements of right cerebral cortex quadrant. Error bars represent standard error.

The attenuation coefficient within the cerebral cortex exhibited some variation as a function of depth. As an example, an average depth profile from an area of approximately 200 μm by 200 μm within the cerebral cortex is shown in Figure 2.6. During baseline the attenuation coefficient had a median value of 1.2 mm^{-1}. After water intoxication this value decreased to approximately 1.1 mm^{-1}. The percent difference between these two profiles as a function of depth is shown of the right y-axis and resulted in an average percent difference of -12%.

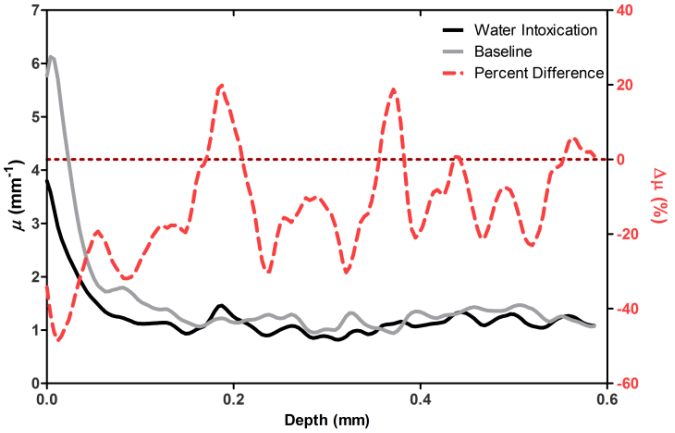

Figure 2.6 Attenuation depth profile from a small region of cerebral cortex. The gray line represents the values during baseline and the black line represents the same depth profile after water intoxication. The percent difference between the two profiles is shown by the red dotted line on the right y-axis. The average percent difference over the entire depth profile was -12%

The rate of change of the attenuation coefficient was calculated for the baseline (defined as the first twenty minutes of the edema experiment) and for edema (post IP injection) by fitting the data using linear regression (Figure 2.7). These rates of change were also compared with the control experiments. A t-distribution test was performed to compare the rates of change. Statistical analysis identified that the rate of change during edema was statistically significant ($p < 0.05$) from both the control ($p = 0.0148$) and the baseline ($p = 0.0135$). As expected, the rate of the change in attenuation coefficient during the control was not statistically different from baseline. These results indicate that the progression of edema can be identified by measuring a rate of change in attenuation coefficient.

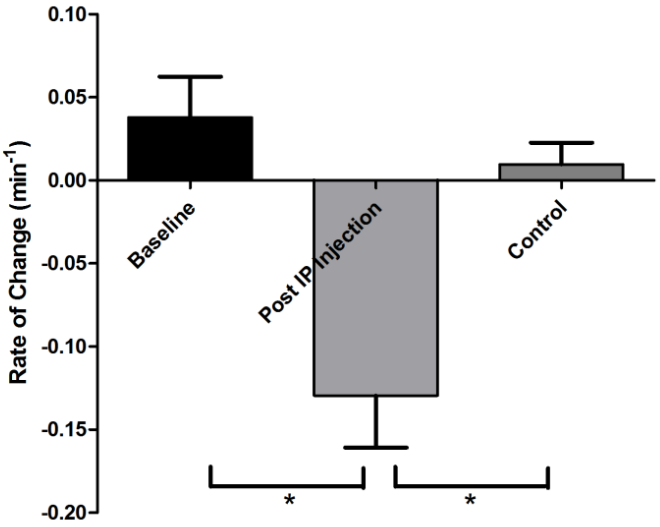

Figure 2.7. Rate of change in average attenuation coefficient during baseline, edema (post IP injection) and control experiments.

Consistent with previous reports using this mouse model, the severity of cerebral edema monotonically increased over time [53]. Analysis of the cerebral blood flow confirmed that flow decreased near the end of the experiment before the animal expired (Figure 2.8). The flow initially increased quickly after the IP injection was administered, presumably due to the injection itself increasing circulating blood volume, and small capillaries became increasingly visible. After approximately 45 minutes post IP injection, the flow began to slow; at the end of the experiment minimal flow was visible in the MIP images (Figure 2.8). The decrease in flow is consistent with the Monro-Kellie doctrine, which states that the cerebral blood volume decreases to compensate for an increase in brain volume [48]. Using DOCT we are able to detect when this volume compensation process is occurring.

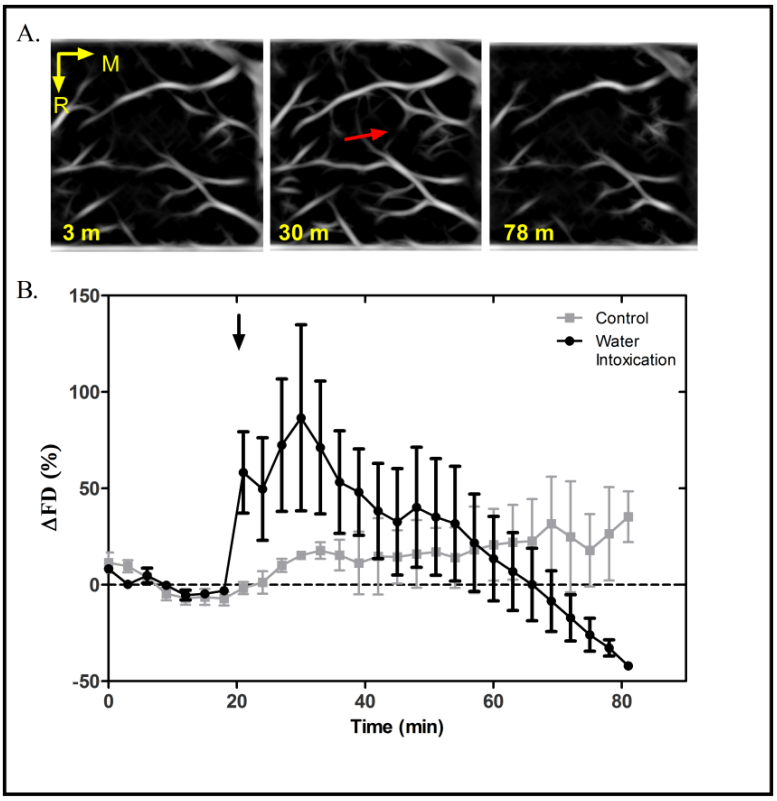

Figure 2.8 (A) MIP *en face* images of the cerebral vascular network created from DAOCT data. Orientation is specified by (R) rostral and (M) midline arrows. Time points are labeled in the bottom left corners. The red arrow indicates an area where capillaries became increasingly visible after IP injection compared to baseline. (B) Percent change in flow density as a function of time.

2.3.2. Local attenuation coefficient trends

The spatial specificity afforded by volumetric OCT data allowed for the optical properties of local regions to be interrogated. The imaging volume was divided into smaller ROIs to investigate the attenuation coefficient trends as (1) a function of distance from midline, (2) from rostral to caudal and (3) axial location. The water intoxication model used in these experiments is a global model of cerebral edema, causing the entire brain to become edematous. The attenuation trends within these localized regions confirmed the global

nature of this model, as each of the ROIs demonstrated the same decrease in attenuation following water intoxication with no statistical difference at various sagittal, coronal or axial positions (Figure 2.9). The ability to interrogate local regions and assess how specific areas within the brain are affected by edema with OCT illustrates the value of optical detection over standard methods of ICP and BWC measurements, which only offer a global assessment.

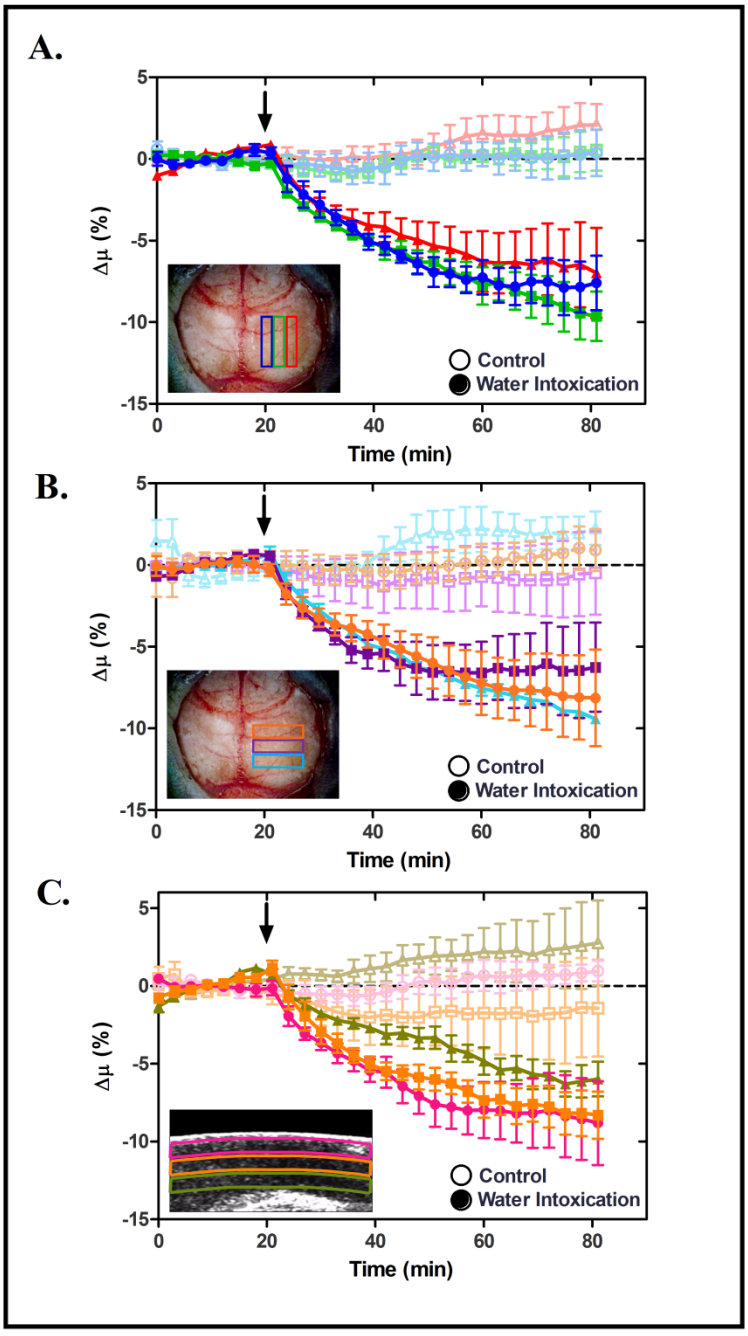

Figure 2.9 Percent change of average attenuation coefficient in the cerebral cortex from three regions spanning (A) medial-lateral, (B) rostral-caudal and (C) axial positions (ROIs shown in inset). Arrow indicates IP injection.

2.4. Conclusion

We demonstrated the ability of OCT to detect cerebral edema based on changes in optical attenuation and cerebral blood flow. During late-stage edema when the cerebral blood flow had considerably slowed due blood vessel compression, the average attenuation coefficient of the cerebral cortex had decreased by 8%. Furthermore, the attenuation began to decrease within minutes of the IP injection and became significant ($p < 0.0001$) from baseline 7 minutes after injection. It is important to note that ICP measurements do not indicate the presence of cerebral edema until more than 20 minutes after the IP injection in the same animal model [53]. Optical detection of cerebral edema with OCT, therefore, can offer an earlier detection time compared with the current practice of using ICP.

The major advantage of OCT detection of cerebral edema is the extremely high spatial resolution it can offer compared to other available techniques. ICP and bulk BWC measurements can only offer a global assessment of edema. Additionally, using diffuse reflectance measurements to detect edema [52,53], which has improved specificity compared to ICP and BWC, has a lower resolution than OCT and lacks any depth discrimination. This technique could therefore be used for detection in a global model of edema, but would be much more difficult to apply to focal models of edema since the optical properties would vary heterogeneously throughout the tissue relative to the site of injury. OCT imaging of a focal edema model would be capable of providing measurements of spatially-resolved optical properties of the brain and make it possible to

build a 4D representation of how the optical properties vary in space and time. Further studies could include OCT-based edema detection in focal models of cerebral edema, such as following controlled cortical impact (CCI) injury in a model of mild traumatic brain injury. In such focal models, not only the spatial but also the temporal resolution of OCT may allow for more precise and early diagnosis of localized brain tissue injury, as well as offer insight into water movement.

We have demonstrated the ability of OCT to detect optical changes correlated with cerebral edema in an *in vivo* water intoxication model. The optical properties of the cerebral cortex were altered as cerebral edema progressed, resulting in a decrease in average attenuation coefficient. DOCT also detected a decrease in cerebral blood flow due to blood vessel compression during severe brain swelling. Localized analysis of attenuation trends determined that detection can be achieved from small regions of brain tissue, highlighting the potential of OCT for 3D spatial monitoring of cerebral edema over time.

Chapter 3. Using optical coherence tomography for detecting optical changes following mild traumatic brain injury

3.1. Introduction

Traumatic brain injury (TBI) is described as any jolt or impact to the head that disrupts normal brain function [63]. Causes of TBI vary widely and include events of rapid acceleration/deceleration, which are commonly experienced during motor vehicle accidents and sports related injuries, as well as contusion and explosive blast injuries, which have become a signature wound of modern warfare [44,64]. The Centers for Disease Control and Prevention (CDC) estimated in their 2010 report to Congress that 2.5 million people visit the emergency department for TBI related injuries each year. Nearly 87% of these cases were treated and released from an emergency department while 11% were hospitalized before being discharged and 52,000 cases led to death [63]. With these staggering statistics, TBI has gained the reputation as being a "silent epidemic" because while a large proportion of people will sustain a TBI, the public awareness of the long-term neurological consequences is largely limited and only recently started gaining more wide spread attention, especially in the context of sports related injuries.

Immediately following a TBI temporary loss of consciousness, memory loss and impaired sensory function (i.e. blurred vision, or change in hearing) are fairly common occurrences. Long term functional changes typically accompany moderate and severe TBIs and include a wide variety of symptoms such as fatigue, long term decrease in

sensory function, impaired attention and concentration, decreased memory and learning ability, and seizures [65]. Behavior and emotional changes such as increased irritability, anxiety and depression are also observed, but such symptoms are not often linked to the TBI (either by the individual or the physician) since these changes are more subtle and difficult to identify and diagnosis [65]. These symptoms have also been increasingly linked to mild TBIs (mTBI) which contrasts the previously held view by doctors and patients alike that complete recovery from a mild injury occurs within a few weeks. Although the injury is classified as "mild" based on initial injury characteristics such as duration of loss of consciousness, the neurobehavioral sequelae that can results from mTBIs are anything but mild. While a majority of those experiencing a mTBI will fully recover 3-6 weeks after the injury, a significant minority of that population will have prolonged cognitive and behavioral dysfunction that affects their quality of life [65–67].

3.1.1. Diagnosis and pathophysiology of TBI

A TBI diagnosis is made if the patient has experienced any loss or decrease of consciousness, any memory loss immediately before or after the injury, and any signs of other neurological effects such as change in vision or speech or loss of balance [63]. The severity of the injury can be classified as mild, moderate or severe as determined by neurological symptoms assessed using the Glasgow Coma Scale (GCS), a scoring system used by physicians to assess the level of consciousness post TBI. In moderate or severe TBI, computed tomography (CT) or magnetic resonance imaging (MRI) can be used to

confirm structural damage and determine the extent of injury [68]. However, structural damage acquired from mTBI cannot be detected by current imaging techniques [69].

Damage to the brain following a TBI is typically classified as primary or secondary. Primary injury describes the direct structural damage sustained immediately after the injury occurred due to the mechanical forces applied to the cranium that results in axonal injury and cell death. Secondary damage is caused by the cascade of biochemical events triggered by the initial injury that lead to further damage in the peri-contusional site that surrounds the initial site of injury. The secondary injury is caused by a combination of many factors including increased BBB permeability, altered ionic balance, oxidative stress, mitochondria dysfunction and decreased tissue perfusion which in turn lead to edema formation, ischemia, raised ICP and further neuronal death [70,71]. In the case of mTBI (defined as having a GCS score > 12 and loss of consciousness less than 30 minutes) the injury is often diffuse in nature rather than at a focal site of injury. As such, diffuse axonal injury, edema formation and changes in blood perfusion all occur on a microscopic scale and go undetected by neuroimaging techniques such as MRI and CT, which can only detect these symptoms on a gross level [67]. Therefore, while mTBI accounts for the majority of TBI injuries (upwards of 75% of all TBIs annually [67,72]), the diagnostic measures used to classify TBI, namely GCS, duration of lack of consciousness and neuroimaging, are geared toward moderate to severe injuries, with mild injuries represented by minimal presence of clinical symptoms and lack of neuroimaging markers. Hence while these tools and symptom checklists can be used to diagnosis mTBI, they lack the necessary details about the structural damage sustained

that would allow a physician to make an informed prognosis about brain function recovery and risk for development of long-term neurocognitive dysfunction [67].

3.1.2. Role of edema in TBI

Edema is one of the major contributing factors to the morbidity and mortality rates for TBI, with some studies reporting that it may account for up to half of deaths occurring after TBI [47,73,74]. Cellular swelling (resulting from cytotoxic edema) changes the intracellular ion and metabolite concentrations which has detrimental effects on cellular function. Additionally, the increased permeability of the BBB after injury results in vasogenic edema, which leads to increased ICP, compression of blood vessels, decreased tissue oxygenation and in severe cases brain shift and herniation. The respective contributions of vasogenic edema and cytotoxic edema to brain swelling following TBI has been a long standing question in TBI research aimed at curbing the effects of edema. Early reports cited vasogenic edema as the main contributor to edema formation. However, more recent studies utilizing clinically relevant TBI models have revealed that both vasogenic and cytotoxic modes contribute to edema, with vasogenic edema occurring over the first minutes and hours after injury while cytotoxic edema forms slowly over the next few days to weeks [75]. The closure of the BBB occurs slowly over the course of days, resulting in a mixed vasogenic/cytotoxic phase occurring during a few days after injury [47].

3.1.3. Imaging of mTBI

Despite the presence of structural damage and increasing evidence of long-term cognitive, functional and emotional symptoms caused by mTBI, CT and MRI are only able to detect abnormalities in a small minority of cases [76]. The vast majority go undetected, leaving physicians without any radiological evidence of structural damage with which to guide diagnosis and treatment. The standard imaging techniques lack the sensitivity and resolution for detecting structural changes following mTBI.

New experimental neuroimaging methods are continuously being explored in an effort to develop techniques sensitive to characteristic factors of mTBI including diffuse axonal injury (DAI), functional changes, and other chemical biomarkers associated with mTBI. Diffusion tensor imaging (DTI) is an extension of MRI that has shown potential for mTBI detection. DTI measures water diffusion in multiple directions at each voxel, which allows for a directional measurement of water diffusion, quantified by the fractional anisotropy, to be made. Typically water diffusion occurs in a defined direction correlated with the direction of fiber tracts. A decrease in the fractional anisotropy implies that water diffusion lacks a strong directionality and is interpreted as a loss of white matter integrity. Numerous studies have been done using DTI for mTBI detection (see Shenton *et al.* for a thorough review [77]). While many have observed differences in mTBI patients, there has been a large amount of variability in the methods used for analysis, the brain regions analyzed and the specific changes observed (i.e. decrease or increase in fractional anisotropy). These results taken together seem to suggest that DTI may be able to achieve the increased sensitivity necessary to detect subtle changes in the

brain caused by mTBI. However, further work is needed to understand the biological implications of the changes observed and longitudinal studies are necessary to correlate DTI findings to neurocognitive outcome.

Functional MRI (fMRI) has also been used to study mTBI and assess brain function and connectivity. This technique measures the ratio of oxy- and deoxyhemoglobin, which is affected by neuronal activity and metabolic demand. Reports from working memory tests and higher-order cognitive functioning tests conducted on human subjects have found areas of hypoactivation following mTBI as well as areas showing hyperactivation, suggesting a possible compensatory mechanism [78]. However, more studies are needed to account for the heterogeneity among the results as well as assess the effects of pharmaceuticals commonly used to treat mTBI, on the fMRI signal [78]. Other imaging modalities including positron emission tomography (PET), magnetic resonance spectroscopy (MRS) and single photon emission computed tomography (SPECT) are also being explored in mTBI imaging [76]. However, while some studies have shown that these techniques can detect potential correlates to injury, all have found difficulty with interpretation of the signal as it relates to the underlying physiology and sensitivity across the wide spectrum of mTBI-type injuries [76,79].

A higher resolution imaging technique can potentially improve mTBI detection, since these injuries characteristically occur on the microscopic scale and current clinical imaging techniques of CT and MRI can only detect changes on a gross anatomical scale. OCT has resolution on the order of 10 μm and could be sensitive to small structural

changes. The work presented in this chapter explores the use of OCT for imaging mTBI *in vivo.*

3.2. Experimental methods

3.2.1. *In vivo* model of mTBI

A controlled cortical impact (CCI) injury model was used to induce mTBI for *in vivo* mouse studies. The CCI device uses an electromagnetic force to drive a piston into the brain at a precise velocity and penetration depth. Neuropathological evaluations of CCI models have determined that axonal injury, loss of BBB integrity, subdural hematoma formation and cortical tissue loss occur following CCI [80]. The severity of these injuries can be regulated by the user defined mechanical parameters for impact velocity, depth of impact and the dwell time of the impactor tip.

Female CD1 wild type mice 8-10 weeks old were anesthetized with an IP injection of a mixture of ketamine/xyalzine mixture (80 mg/kg ketamine, 10mg/kg xylazine). A 4 x 4 mm craniectomy was performed over the left and right cerebral cortex leaving the dura intact (the borders of which were formed by the coronal suture and lambdoid suture in the anterior-posterior direction and midline and temporalis attachment in the medial-lateral direction). After securing the mouse onto a stereotaxic frame, the animal was subjected to a mTBI via CCI (Leica Impact One Stereotaxic Impactor) with a 1.5 mm diameter impactor tip that was discharged at a velocity of 4 m/s with a contact time of 200 ms at an impact depth of 0.3 mm (Figure 3.1). The depth was controlled by using a contact sensor to indicate the exact point of contact while the impactor tip was in

the extended position. The impactor tip was then retracted and the device was lowered by 0.3 mm before impact to achieve the desired depth. The angle of the impactor tip relative to the surface of the brain was varied to compare two distinct injury groups, one of which exhibited subdural hemorrhage (achieved with an angle of 22°) and a second group that had minimal visible bleeding at the site of injury (angle 26-28°) (Figure 3.2). The impact parameters are summarized in Table 3.1. Three animals were used for each impact group. Additionally, two sham control experiments were performed.

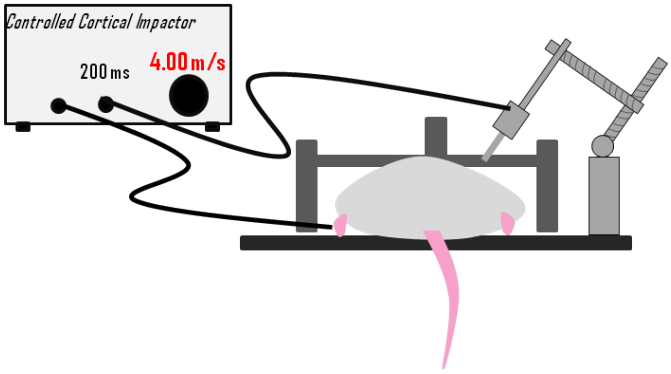

Figure 3.1 Schematic of CCI setup. The mouse is secured in stereotaxic frame with the impactor tip centered over the right cerebral cortex. The impactor is connected to the CCI device controlling the velocity and impact depth. The contact sensor is pressed to hind limb to indicate when impactor tip makes contact with the dura.

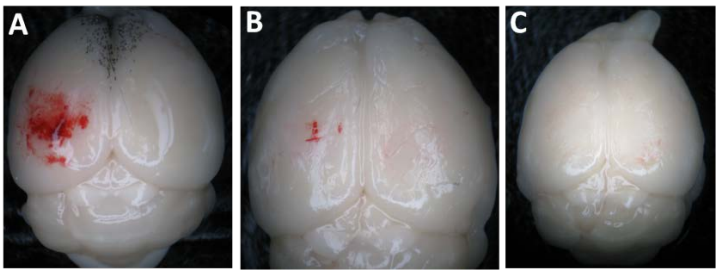

Figure 3.2 Representative images of postmortem dissected brain (A) following CCI with shallow impact angle, (B) following CCI with greater impact angle and (C) sham animal.

Table 3.1 CCI Parameters for two groups of impacted animals, the first of which showed more bleeding (MB group) and the second which had considerably less bleeding (LB Group).

	MB Group	**LB Group**
Velocity (m/s)	4	4
Dwell time (ms)	200	200
Depth of impact (mm)	0.3	0.3
Angle of impactor	22°	26-28°

3.2.2. *OCT image acquisition*

After the mouse was prepared for CCI and secured in a stereotaxic frame as described above the animal was positioned in the sample arm of the SD-OCT setup (described previously in section 2.2.5). The imaging volume spanned 4 mm rostral-caudal and 7 mm laterally covering both the ipsilateral and contralateral sides, approximately centered on midline. Each B-scan contained 2048 A-lines, acquired at a rate of 15 kHz, and was oriented in the sagittal direction. Each volume consisted of 250 B-scans and volumes were acquired at an interval of five minutes. Thirty minutes of baseline recordings were collected. The animal, which was sitting on a vertical translation stage,

was then lowered away from the optics of the OCT sample arm to allow for the CCI device to be positioned over the right cerebral cortex. The impact was applied and the stage was then translated back to its original height for continued imaging. OCT data was collected for 1.5 hours after impact.

3.2.3. Histological analysis

Following OCT imaging, the animals were deeply anesthetized with an IP injection of ketamine xylazine combination and transcardially perfused with ice-cold PBS followed by 4% paraformaldehyde (PFA). The brains were rapidly dissected, post-fixed overnight in 4% PFA in 4° C and followed by cryoprotection in 30% sucrose in PBS at 4° C. Coronal sections, 50 μm thick, were cut with a cryostat (Leica CM1950, Leica Microsystems) and stored in PBS at 4° C. Sections were blocked with 5% normal goat serum in 0.1M PBS and incubated with primary antibody to Albumin (1:100, Abcam), in 0.3% Triton X-100 at 4° C overnight. The sections were then washed with PBS, incubated with species-specific secondary antibody conjugated with Alexa 594 for visualization and counterstained with Neurotrace Fluorescent Nissl Stains (1:10, Life Technologies) for 5 minutes followed by PBS wash. Sections were then mounted in Vectorshield (Vector Laboratories). Images of the ipsilateral and contralateral cortex were taken using a fluorescence microscope.

3.2.4. OCT optical attenuation analysis

The depth resolved optical attenuation coefficient was calculated (described previously in section 2.2.6) at each pixel in order to quantify the attenuation and how it changes following mTBI both spatially and temporally. The imaging volume spanned the ipsilateral and contralateral hemispheres of the brain and the image data from each side was analyzed separately by dividing the imaging volume based on visual analysis of the post-processed OCT images. The average attenuation coefficient within the tissue contained in the top 600 um (containing only gray matter) was calculated at every time point. Areas exhibiting blood flow in the DOCT images were excluded from the analysis by using a threshold to identify pixels that contained blood flow and subsequently removing these pixels from the average attenuation calculation. Blood exhibits higher optical attenuation compared to tissue. Therefore, removing areas exhibiting flow reduced the contribution of vascular changes to the overall average attenuation value calculated and ensured that this number was primarily reflecting scattering changes occurring in the brain parenchyma.

3.3. Results of mTBI model

3.3.1. Average optical changes detected in the cerebral cortex

The percent change from the average baseline attenuation coefficient value was calculated as a function of time for the group with more bleeding (MB Group), with less bleeding (LB Group) and the sham group. The sham group, which underwent a bilateral

craniectomy but received no impact, demonstrated a monotonically increasing trend in the attenuation coefficient over the course of the two hour experiment. This change seemed to be related to the craniotomy, as they were not observed for thinned-skull preparations. In order to assess the differences caused specifically by the impact, the average trend observed in the sham group was subtracted from the percent change values calculated for the impact groups. Both the MB group and LB group demonstrated changes in the average attenuation coefficient that were different from the changes observed in the sham animals. On the ipsilateral side, each group demonstrated an initial increase directly after impact, with the MB group exhibiting a larger increase compared to the LB group. A decreasing trend was then observed within 20-30 minutes after impact, which continued through the end of the experiment (Figure 3.3). The contralateral side also showed a small increase after impact and showed larger variability among grouped animals compared to the variability observed on the ipsilateral side, but these changes are not statistically different from baseline values (Figure 3.4).

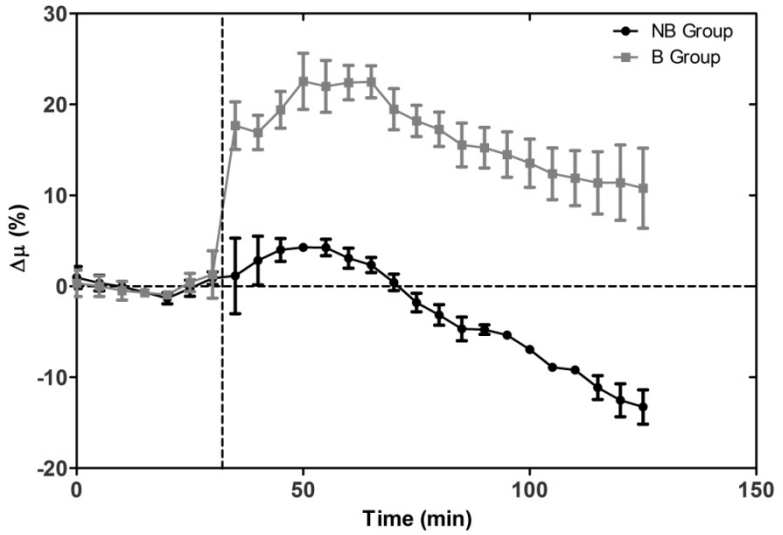

Figure 3.3 Percent change in average attenuation coefficient on the ipsilateral side, shown with the sham trend subtracted, for the LB and MB impact groups. The vertical dotted line indicates the time of impact.

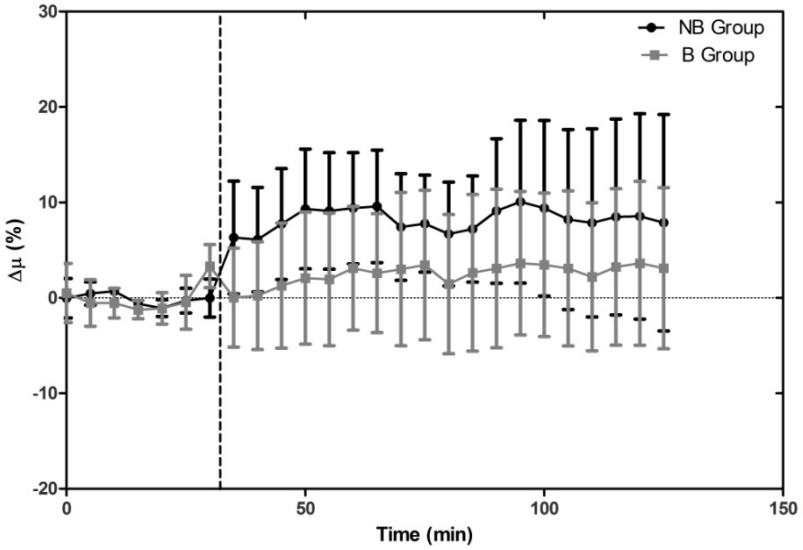

Figure 3.4 Percent change in average attenuation coefficient on the contralateral side, shown with the sham trend subtracted, for the LB and MB impact groups. The vertical dotted line indicates the time of impact.

3.3.2. Local sites of injury

Local areas in the cortex that showed a change in optical attenuation were observed in volume renders of the depth-resolved attenuation data. Comparison of time-lapse volume renders from both the MB group (Figure 3.5) and LB group (Figure 3.6) demonstrated areas of increased attenuation around the impact site. The areas showing increased attenuation occur diffusely rather than exhibiting strong edges or boundaries, similar to that observed in the albumin histology images (see section below). No such changes are observed in the contralateral sides or on either side on the sham volumes (Figure 3.7). These results indicate that OCT can provide visual confirmation of injury following mTBI in addition to the quantitative changes shown in the previous section.

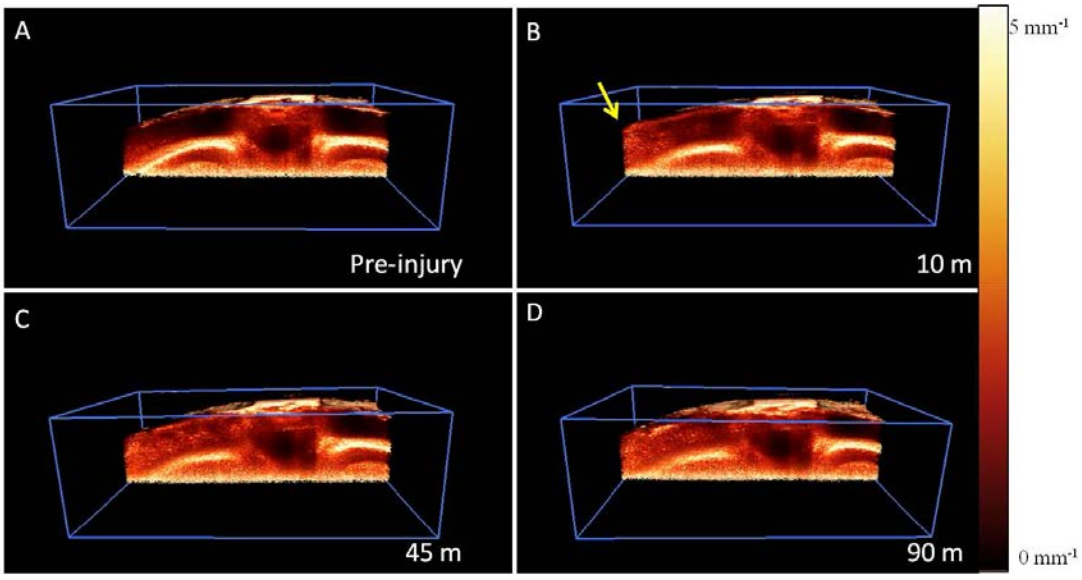

Figure 3.5 Representative volume renders in a coronal orientation from MB group animal for (A) pre-injury state, (B) 10 minutes, (C) 45 minutes and (D) 90 minutes after injury. Ipsilateral side is shown on the left. Arrow points to area showing increase in attenuation following injury.

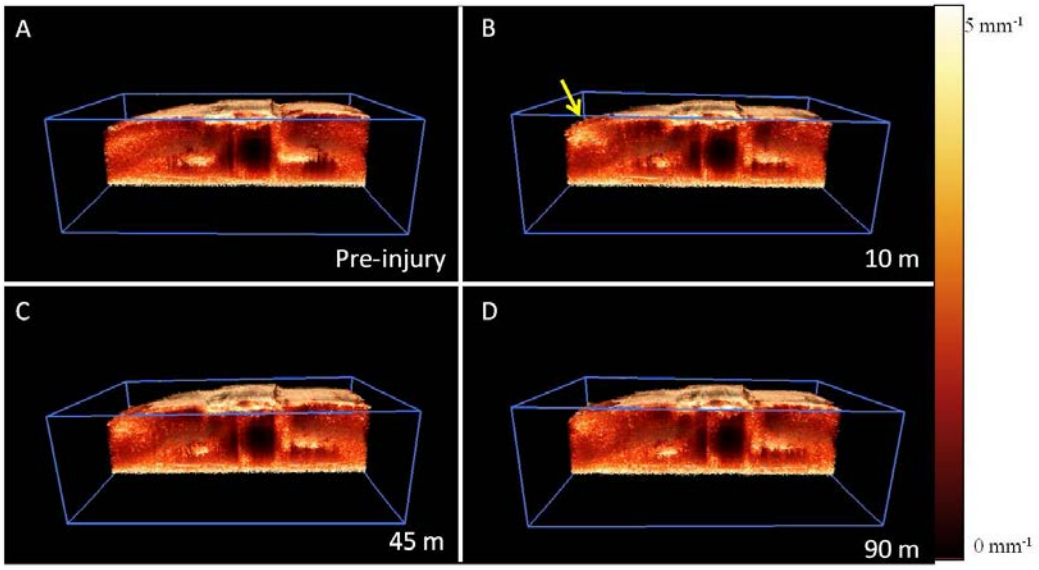

Figure 3.6 Representative volume renders in a coronal orientation from LB group animal for (A) pre-injury state, (B) 10 minutes, (C) 45 minutes and (D) 90 minutes after injury. Ipsilateral side is shown on the left. Arrow points to area showing increase in attenuation following injury.

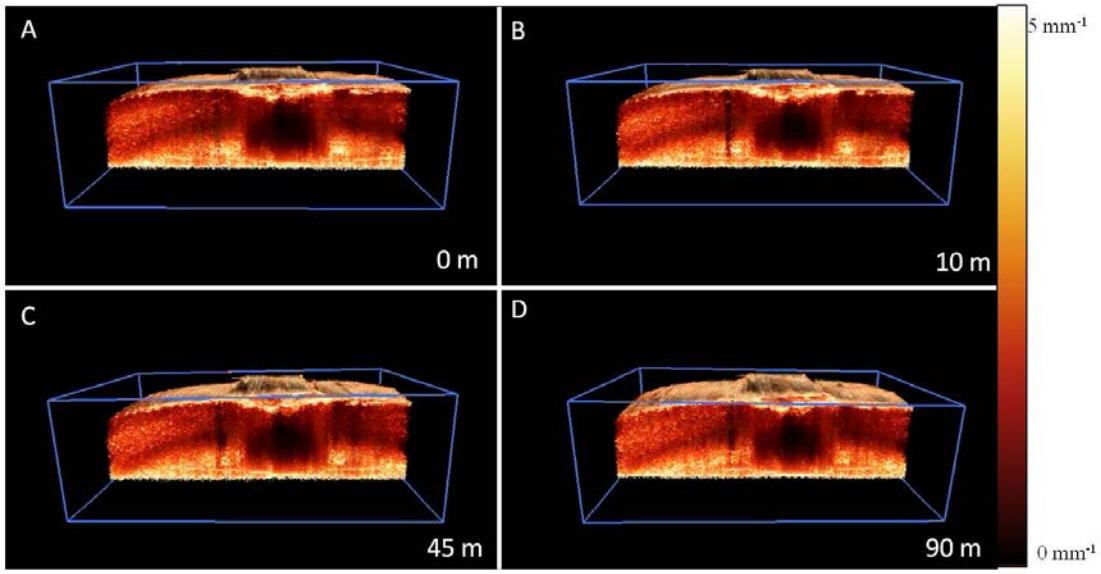

Figure 3.7 Representative volume renders in a coronal orientation from a sham animal for (A) 0 minutes, (B) 10 minutes, (C) 45 minutes and (D) 90 minutes of imaging.

3.3.3. Histology

Histological staining of the brain tissue after impact revealed loss of BBB integrity in both the MB and LB groups. Albumin extravasation was observed in the ipsilateral cortex of both impact groups, as indicated by the presence of the albumin stain shown in red in Figure 3.8. These results show that vasogenic edema was present following impact. The Nissl stain confirms that wide spread cell death did not occur during the first hours after injury, consistent with typical mTBI.

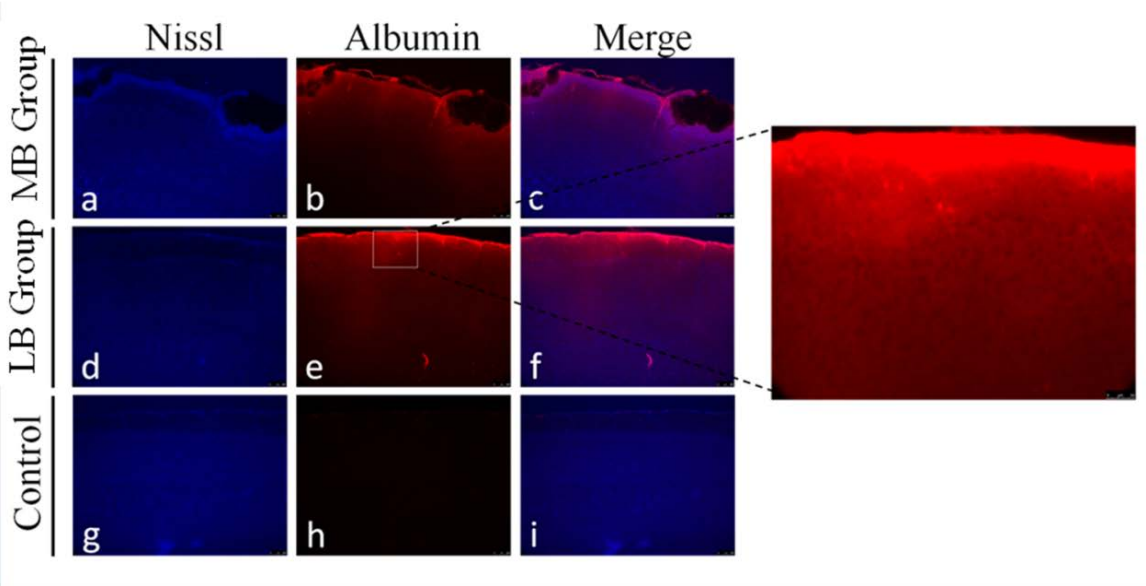

Figure 3.8 Immunohistochemical staining for albumin (red) and Nissl counterstain (blue) in the ipsilateral cortex after impact for MB group (a-c), LB group (d-f) and control (g-i). Images (a-i) were taken at 10x. Zoom image was taken at 20x.

3.4. Discussion and conclusion

In this study we examined the changes in the optical attenuation of the cerebral cortex following mTBI using OCT. Using a CCI model of mTBI, the ipsilateral side demonstrated changes in attenuation in animals that experienced subdural bleeding as well as those that displayed very little bleeding. These changes were quantified by calculating the average attenuation coefficient in the cortex. Additionally local changes were visually evident through volume renders of the data. Histological analysis revealed that the BBB integrity had been compromised, leading to the formation of vasogenic edema.

The initial increase and subsequent decrease observed in the average cortical attenuation on the ipsilateral side may be the result of a combination of blood seeping into the tissue as well as the formation of edema. The initial increase was larger in the MB group compared to the LB group. Blood is highly attenuating and therefore this may account for the initial increase/offset observed directly after impact. The slow decreasing attenuation trend observed starting 20-30 minutes after impact, consistent with our data from global edema experiments presented in Chapter 2, may indicate that vasogenic edema formation. The contralateral side did show a large amount of variability in the average cortical attenuation value across experiments, but these changes were not statistically different from baseline. It is not yet known how much the contralateral side of the brain is affected by mTBI. Our results indicate that it may be subtly affected. However more experiments would be necessary for statistical analysis.

Mild TBI is very difficult to detect using current clinical imaging techniques, which seem to lack the sensitivity and resolution for detecting mild structural changes. The results presented in this chapter demonstrate that OCT has the ability to detect optical changes in the cortex following mTBI. Visual comparison of OCT volumetric data taken after impact compared to uninjured samples demonstrate noticeable differences. Additionally, quantification of the change in optical attenuation throughout the ipsilateral cortex was statistically different from baseline values and demonstrated interesting dynamics related to loss of BBB integrity and edema formation. These results highlight the potential for OCT to detect mTBI and monitor focal edema progression.

Chapter 4. Development of differential-absorption OCT system for local brain water content analysis

4.1. Introduction

In complex models of edema, such as TBI discussed in the previous chapter, it can be difficult to interpret the exact cause of the optical attenuation changes observed because there are many biological processes happening simultaneously. In order to more precisely isolate changes correlated to fluctuations in local water content, additional information is needed. The optical attenuation measured from our SD-OCT system centered at 1300 nm is primarily dominated by scattering, as absorption by biological constituents in this wavelength range is relatively small. However, the scattering and absorption properties of a sample each provide unique information about the chemical composition of the material and these properties can be leveraged to increase the sensitivity of our OCT to water.

When light enters a sample, it can be scattered, absorbed or pass directly through the material. The likelihood of a scattering or absorption event happening depends on the wavelength of the light, the shape and size of the scatterer relative to the wavelength, and the chemical composition. The attenuation coefficient, μ, of the material provides a macroscopic measure of scattering and absorption, and is the sum of the scattering coefficient (μ_s) and absorption coefficient (μ_s) of the material. This is described as a function of distance traveled through the material, *z*, by the Beer-Lambert law:

$$\frac{I(z)}{I_o} = e^{\int_0^z \mu(z)dz} \qquad \textit{(Eq. 4-1)}$$

$$\textit{where } \mu(z) = \mu_a(z) + \mu_s(z) \qquad \textit{(Eq. 4-2)}$$

Scattering and absorption are both wavelength-dependent phenomena. The scattering coefficient of a material tends to be a slowly varying function of wavelength while the absorption coefficient typically contains peaks over narrow wavelength bands. These narrow bands are centered on wavelengths that either carry energy equal to the energy difference between ground and excited states of outer orbital electrons or equal to the energy of a vibration state of the molecule. Since the wavelengths absorbed by a material are directly related to the chemical composition, measuring the absorption provides a way to measure the concentration of specific molecules, such as water, contained in a sample. In this way, the work presented in this chapter is aimed at using OCT to measure the absorption properties of a sample in the wavelength range near the 1450 nm absorption band of the water molecule in order to more precisely measure edema formation.

4.2. Principle of DA-OCT

The idea of using OCT to interrogate the absorption properties and chemical composition of a material was first proposed in 1998 [81]. This technique, known as differential absorption OCT (DA-OCT), compares two OCT images acquired from two separate light sources; one source emits in an absorption band of the chemical of interest while the second source emits just outside of the absorption band. The analysis requires calculating a differential image from the intensity images of each light source. Pircher *et al.*

demonstrated this technique by measuring the water concentration of the cornea *in vitro* using light sources centered at 1300 nm and 1488 nm [82]. Following their convention, the measured OCT signal is proportional to the square-root of the reference and sample arm intensities

$$S_{OCT}(z) = C\sqrt{I_r I_s(z)} \qquad \textit{(Eq. 4-3)}$$

where, *C* is a constant. Using *Eq. 4-1*and *Eq. 4-2*, the sample intensity in Eq. 4-3 can be rewritten in terms of the incident intensity and the scattering and absorption coefficients:

$$ln\big(S_{OCT}(z)\big) = ln\left(C\sqrt{I_r}\right) + \frac{1}{2}ln\big(I_s(z)\big) \qquad \textit{(Eq. 4-4)}$$

$$= ln\left(C\sqrt{I_r}\right) + ln(I_o) - z(\mu_a(z) + \mu_s(z)) \qquad \textit{(Eq. 4-5)}$$

Note that the double pass geometry of OCT imaging has been accounted for in this expression. For DA-OCT, the two OCT images are formed using two light sources with different center wavelengths. Assuming the light sources have the same focal plane within the sample, the difference between the signals obtained from each source is given by:

$$ln\big(S_{OCT}(z,\lambda_1)\big) - ln\big(S_{OCT}(z,\lambda_2)\big) = ln\left(\frac{I_r(\lambda_1)I_o(\lambda_1)}{I_r(\lambda_2)I_o(\lambda_2)}\right) - (\Delta\mu_a + \Delta\mu_s)z \qquad \textit{(Eq. 4-6)}$$

where $\Delta\mu_a$ and $\Delta\mu_s$ represent the difference in the scattering and absorption coefficients for each wavelength. Assuming the reference intensity and incident intensity on the sample are constant during imaging, the first term in Eq. 4-6 is constant. Therefore, the difference in the OCT signal obtained at each wavelength is a linear function of *z*, where

the slope is the sum of the differential absorption and scattering coefficients and the offset is determined by the reference and sample intensity. The absorption information is retrieved by choosing wavelengths such that $\Delta\mu_s << \Delta\mu_a$, thereby leaving the slope to represent only the difference in absorption at each wavelength. It then follows that high intensity areas in the differential image correspond to areas with large water content. The concentration can be calculated from the slope if the differential absorption cross-section of the pure substance is known [82].

4.3. DA-OCT system design

The DA-OCT system was designed with three criterion in mind: (1) the images formed from each light source must be simultaneously acquired to ensure that the pair of images can be properly compared, (2) the OCT system can toggle between conventional OCT imaging and DA-OCT imaging with minimal hardware adjustments or time-intensive alignment and (3) the new spectrum is focused onto the same line scan cameras used in the normal setup. Since our DA-OCT setup is targeting water absorption properties of various samples, the first light source is centered at 1300 nm (same source used in SD-OCT setup described in previous chapters) and the second light source is centered at 1430 nm, which is within the 1450 nm absorption band of water.

A wavelength division multiplexer (WDM) was used to combine the light from each source in the source arm of our OCT system. This allowed for the light from both sources to then travel to the reference and sample arms through the fiber optic network already in place. The light reflected from each arm then traveled to the detection arm of

the OCT setup. The spectrometer in the conventional OCT system needed to be modified to account for the second light source. The grating/lens combination in the original spectrometer was designed to spread the bandwidth of the 1300 nm light source across the full width of the camera. In order to fit a wider bandwidth resulting from the combination of two sources (approximately 1200-1480 nm) onto the same camera, a new grating and focusing lens was needed. The grating, lens, bandwidth and angles of incidence and transmission all affect the width of the resulting spectrum (Figure 4.1). Using the grating equation, two expressions can be written to describe to desired angular spread in terms of the hardware parameters.

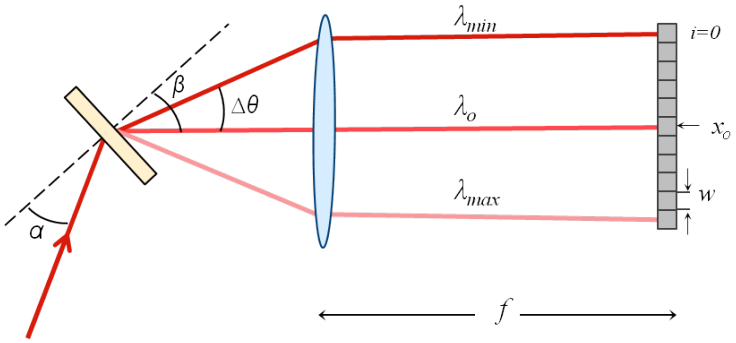

Figure 4.1 Schematic of grating, focusing lens and line scan camera in SD-OCT spectrometer. α: incident angle, β: transmission angle, f: focal length of lens, λ_o, λ_{min} and λ_{max}: middle, minimum and maximum wavelength of combined spectrum, w: pixel width.

$$\lambda_{min} = d \cdot \left(\sin(\alpha) + \sin\left(\beta - \tan^{-1}\left(\frac{-x_o}{f}\right)\right)\right),$$

$$\lambda_{max} = d \cdot \left(sin(\alpha) + sin\left(\beta + tan^{-1}\left(\frac{w \cdot N - x_o}{f}\right)\right)\right) \qquad \textit{(Eq. 4-7)}$$

Solving this system of equations ensures that the choice of grating and lens will produce a spectrum that fits onto the length of the camera. A grating with 600 lines mm^{-1} spacing (Wasatch Photonics) and a 2'' focusing lens with a 150 mm focal length (Thorlabs) was chosen.

4.3.1. Hardware modifications to spectrometer

The spectrometer in our conventional OCT system is equipped for PS-OCT imaging, as shown by the presence of the polarizing beam splitter (PBS) and second camera in Figure 4.2. After the focusing lens in the spectrometer, the light is incident on a PBS that splits the light between two line scan cameras, depending on their polarization state. The spectrometer optics (collimator, grating and lens) could not be moved to accommodate the new DA-OCT spectrometer, since that would disrupt the alignment and therefore day-to-day operation of the conventional PS-OCT system. One possible solution was to focus the DA-OCT spectrum through the open side of the PBS. However, the PBS was designed for transmission only in the direction of incidence shown in Figure 4.2. Initial attempts at alignment of the DA-OCT setup through the open side of the cube showed that the efficiency for operation in this direction did not produce nearly enough measurable SNR.

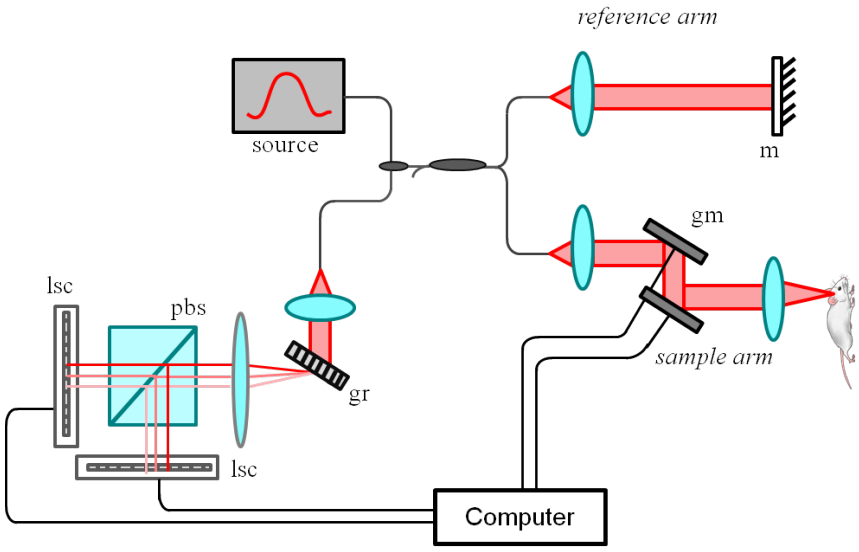

Figure 4.2 PS-OCT system centered at 1300 nm. m:mirror, gm: galvanometer mounted mirror, gr: grating, lsc: line scan camera.

The problem was solved by remounting the PBS on a kinematic base (2'' round, Thorlabs), which utilizes a ball and v-grove design to provide highly repeatable positioning for optical elements that need to be removed and inserted back to the same position. The optics for the DA-OCT spectrometer were positioned opposite from the bottom camera in the diagram and the PBS is always removed from the setup during DA-OCT acquisition. This allows for the full DA-OCT spectrum to be aligned onto the camera. The PBS and second camera are only necessary for PS-OCT imaging to provide an extra mode of contrast and is not currently necessary during DA-OCT imaging.

The final system configuration is shown in Figure 4.3 for DA-OCT operation. The light emitted from each source is combined by a WDM (AC Photonics) and sent through the same fiber optic network used in the normal PS-OCT system. The 1300 nm source provides 4.5 mW incident power on the sample while the 1430 nm delivers

2.9 mW incident power. Light returning from each arm is directed to the detection arm and is sent either to the PS-OCT spectrometer or the DA-OCT spectrometer by switching a single fiber between input ports leading to each spectrometer.

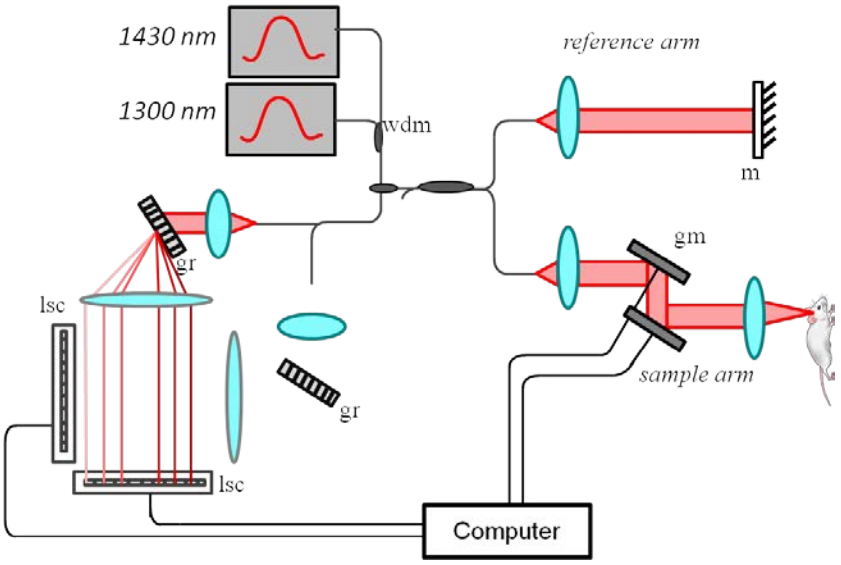

Figure 4.3 Schematic of OCT system configuration that can switch between conventional PS-OCT and DA-OCT imaging (shown in DA-OCT mode). wdm: wavelength division multiplexer, m: mirror, gm: galvanometer mounted mirror, gr: grating, lsc: line scan camera.

4.4. Wavelength calibration and system characterization

A SD-OCT system is typically characterized by performance measures of axial resolution, imaging range and sensitivity drop-off (discussed previously in Chapter 1). Two images are formed from the DA-OCT spectrum by dividing the spectrum at the lowest point between the two Gaussians, as shown by the dotted line in Figure 4.4, and subsequently following the same processing steps for conventional OCT data to produce

an A-line from the spectral information (see Chapter 1). System characteristics were therefore determined for each spectrum separately.

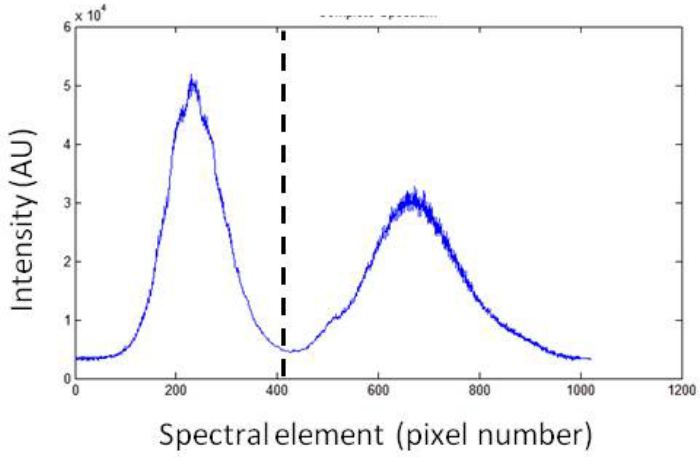

Figure 4.4 Combined spectrum from DA-OCT setup. Dotted line indicates position at which the two spectra are divided and processed into A-lines. The 1430 nm source is shown on the left, 1300 nm source on the right.

Accurate wavelength assignment for each camera pixel is necessary to minimize the axial resolution of the system. Wavelength calibration was achieved by imaging a single reflector to introduce a modulation onto the spectrum. The modulation is a perfect cosine as a function of wavenumber, k (assuming no dispersion) [22]. Therefore, the phase of the modulation when represented as a function of k should be linear; any nonlinearity is due to improper wavelength assignment. In order to achieve the proper wavelength assignment for each camera pixel, an initial estimate was made based on the grating equation and geometry of the setup and the error in phase linearity was iteratively calculated and corrected, as described by Mujat *et al.* [22]. The initial wavelength

estimate was generated for the entire spectrum and then divided to iteratively calibrate each source separately.

Upon calibration, the axial resolution was determined by imaging a mirror in the sample arm and calculating the FWHM of the reflection peak. The 1430 nm system has an axial resolution of 23 μm and the 1300 nm system has a resolution of 12 μm. Note, both systems have a lateral resolution of 20 μm, as this is determined by the focusing lens in the sample arm.

The imaging range of each system is slightly different due to the difference in center wavelength, bandwidth and total number of camera pixels each spectrum covers (see Eq. 1-11). The 1430 nm source has a bandwidth of 45 nm and occupies 466 pixels of the total 1024 pixels. The 1300 nm source has a bandwidth of 120 nm and covers the remaining 558 pixels. The measured imaging range for the 1430 image was 2.11 mm and the 1300 nm was an imaging range of 1.71 mm.

All SD-OCT systems experience a loss of sensitivity with increasing depth due to finite pixel size and cross-talk between pixels (see section 1.2.2). The amount of signal lost with depth depends on the wavelength spacing on the camera and quality of focus. The sensitivity fall-off was determined for each system by imaging a mirror in the sample arm at various depths in the imaging range. The 1430 nm system had a loss of approximately an 8 dB over the range shown in Figure 4.5 while the 1300 nm system had a loss of about 13 dB (Figure 4.6).

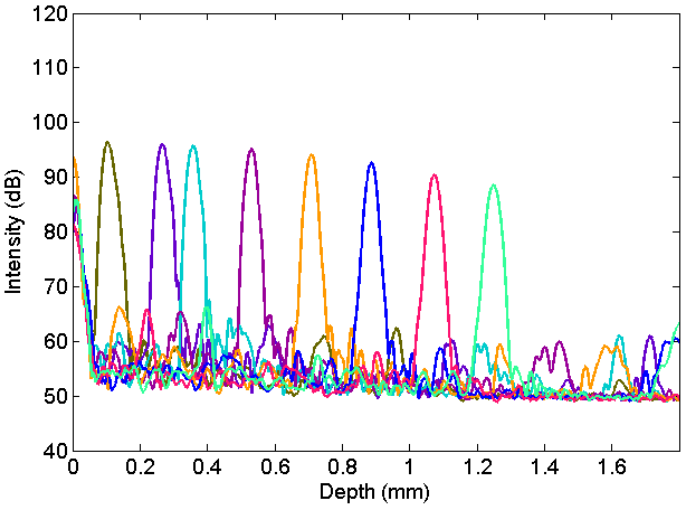

Figure 4.5 Reflections off of a mirror positioned at various heights show the sensitivity fall off as a function of depth for the 1430 nm system in the DA-OCT setup.

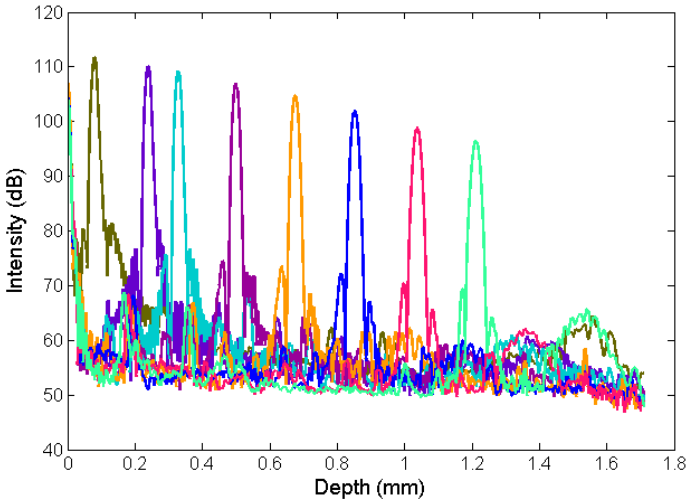

Figure 4.6 Reflections off of a mirror positioned at various heights show the sensitivity fall off as a function of depth for the 1300 nm system in the DA-OCT setup.

4.5. Image processing of DA-OCT data

Retrieving information about the location and amount of water in a sample relies on the fact that the scattering coefficient at the two chosen wavelengths is very similar, while the absorption coefficients are very different. Therefore, by measuring the attenuation coefficient in the sample at each wavelength and then calculating the difference, the differential absorption coefficient can be determined. The attenuation coefficient image was calculated for the 1300 nm image and the 1430 nm image using a recently proposed method for determining the depth-resolved attenuation coefficient from OCT intensity information [61], as described in Chapter 2. A separate correction was applied to the intensity in the 1300 nm image and 1430 nm image to remove the contribution of the sensitivity drop off to the measured attenuation. The differential absorption image was then calculated by subtracting the 1300 nm attenuation image from the 1430 nm image. Since the images were different sizes in depth (both in pixel number and in pixel size), interpolation was used to determine the 1430 nm intensity values at the same points in depth as is represented by each depth point in the 1300 nm image, before the images were subtracted.

4.6. Preliminary data

4.6.1. Dehydration of *ex vivo* tissue

As a preliminary experiment, a small piece of raw chicken was imaged over time as the sample dehydrated. The sample remained in the same position under the sample arm for

the duration of the experiment. The average differential absorption coefficient was calculated in a 3 x 3 x 1 mm volume of tissue. Example OCT intensity images and the differential absorption image is shown in Figure 4.7

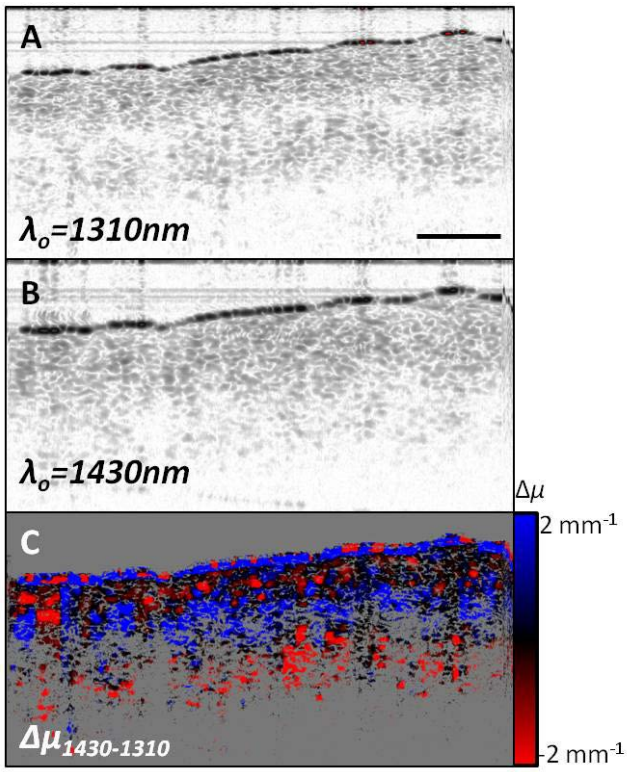

Figure 4.7 OCT imageing of raw chicken sample. (A) 1300 nm intensity image, (B) 1430 nm intensity image and (C) differential absorption image. Scale bar = 0.5mm

The average attenuation coefficient measured for λ_o = 1300 nm and λ_o = 1430 nm is shown in Figure 4.8A. The average value of μ_{1430} was higher than μ_{1300}, as expected due higher absorption at λ_o = 1430 nm. As the sample dehydrated over 45 minutes, the average value of both μ_{1430} and μ_{1300} exhibited dynamic changes. The attenuation at 1430 nm began decreasing rapidly at the start of the experiment while the attenuation of 1300 nm light initially remained stable (Figure 4.8A). The results suggest that initially

when water was leaving the sample, the absorption was largely affected. However, once enough water left the sample, the sample began to contract, which increased the density of scatterers and caused the scattering coefficient to increase. The increase in scattering is more obvious in the μ_{1300} plot compared to the μ_{1430} graph since the attenuation at 1430 nm is influenced by both increased scattering and decreased absorption due to the decrease in water content. The average differential absorption coefficient (calculated from differential attenuation image) is shown in Figure 4.8B. The differential absorption coefficient steadily decreases for approximately 35 minutes. These results demonstrate that the differential absorption coefficient is able to detect changes in water content continuously over time, which is not evident from either attenuation plot alone in Figure 4.8A and demonstrate the increased sensitivity to water content afforded by DA-OCT.

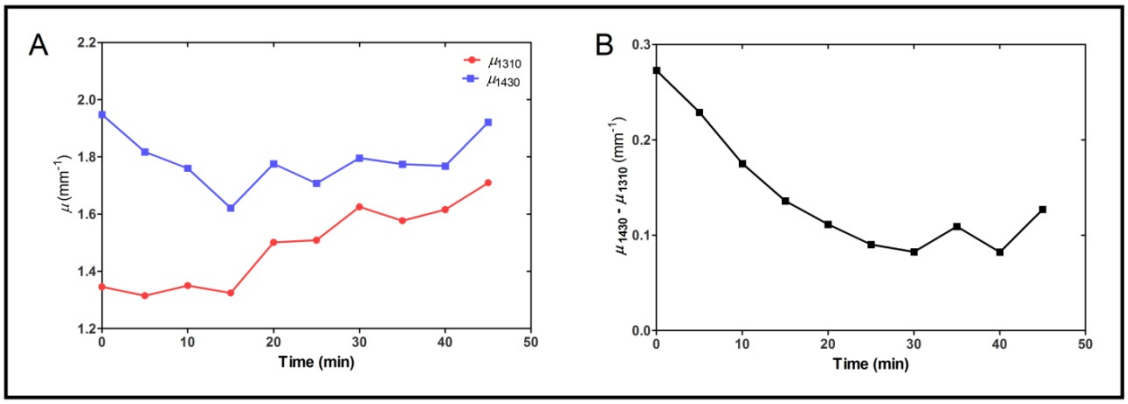

Figure 4.8 (A) Average attenuation coefficient in raw chicken sample over time, measured at λ_o = 1300 nm and λ_o = 1430 nm. (B) Average differential absorption coefficient versus time.

4.7. Conclusion and future directions

In summary, the work presented in this chapter describes the design and implementation of a DA-OCT system aimed at measuring the amount of water in a biological sample by using two light sources, centered at 1300 nm and 1430 nm, to simultaneously image a sample. The resolution, imaging range and sensitivity fall-off were characterized for each light source and algorithms were developed to process the differential absorption image from the depth-resolved attenuation measurements at 1300 nm and 1430 nm. The differential absorption image represents the difference in attenuation of each light source on a pixel-by-pixel basis, which allows for spatial variation in water content to be analyzed. Preliminary results demonstrated that the differential absorption coefficient provides an increase in sensitivity to water content that was not available using data from a single light source. Future work can be done to characterize the sensitivity of the DA-OCT system to changes in water content by quantifying the change in the differential absorption signal and comparing it to known changes in water content. For example, changes in BWC can be precisely quantified using specific gravity techniques of local tissue biopsy samples [83]. The results of these measurements can be compared to the differential absorption coefficient in the same region at various stages of edema development to establish the relationship between water content and differential absorption coefficient. Once the sensitivity of the DA-OCT system has been characterized, focal cerebral edema models of TBI, stroke and tumor can be explored.

Chapter 5. Conclusions and future directions

In summary, the work presented in this dissertation describes the use of OCT for detection of cerebral edema *in vivo.* Cerebral edema occurs when excess water accumulates in the brain. This can occur due to a number of conditions including TBI, infection and stroke, and often contributes to the formation of secondary injuries and increased morbidity and mortality. Intracranial pressure (ICP) monitoring is most commonly employed for cerebral edema monitoring. However, this method only provides a global measure of brain swelling within the cranium and is not able to detect edema when it is first developing. Early, precise detection of brain swelling would be highly advantageous both clinically for guiding prognosis and treatment decisions, as well as in a research setting for studying edema formation and progression in a variety of animal models and evaluating the effect of potential treatments.

In Chapter 2, results were presented from a water intoxication mouse model of cerebral edema. The depth-resolved attenuation coefficient was calculated at every pixel in the OCT image and was used to measure how the optical properties of the cerebral cortex changed during edema progression. The results showed a continual decrease in optical attenuation in the cerebral cortex with increased brain swelling. Additionally, DOCT data confirmed severe brain swelling by detecting vasculature compression. The decrease in optical attenuation became statistically different from baseline within seven minutes of giving the IP injection. In the same mouse model, ICP was not able to detect edema until 20 minutes after injection [53]. Optical detection is clearly advantageous for

early detection as the measured optical signal is directly related to the tissue composition unlike ICP which is nonlinear related to bulk brain volume.

A more clinically relevant, focal edema model was explored in Chapter 3, using a CCI mouse model of mTBI. Volume renders of OCT data provided visual confirmation of mTBI, which is typically difficult to see with current clinical imaging techniques. The average attenuation coefficient in the cortex was calculated to quantify the changes in the optical properties of the tissue. The results demonstrated a biphasic change occurring after injury with an initial attenuation increase followed by a decreasing trend 20-30 minutes later. Two groups were compared that had differing amounts of bleeding following injury. The group that experienced less bleeding had a smaller initial increase compared to the second group, suggesting that this increase was due to increased presence of blood in the tissue. The decreasing trend observed a half hour after injury was reminiscent of the trend observed in the global edema model. Histological staining confirmed loss of blood brain barrier (BBB) integrity in both groups. Hence the decreasing trend was likely caused by vasogenic edema formation.

Chapter 4 discussed OCT system modifications designed to increase the sensitivity of our OCT signal to water content. A DA-OCT setup was implemented by incorporating a second light source centered at 1430 nm into our existing 1300 nm SD-OCT setup. The spectrometer was modified to include a second grating/lens combination that focused the entire DA-OCT spectrum onto a single camera in the existing setup. During post-processing, the DA-OCT spectrum was divided to separate the data by light source and then an intensity image was formed for each wavelength band. An

attenuation image was then calculated from data for each wavelength band and the difference between these two images resulted in the differential absorption image that is sensitive to changes in water content. Preliminary results of dehydrated *ex vivo* tissue demonstrated that the DA-OCT signal detected changes in water content over a longer period of time than was evident from data processed from either light source alone. The increase in sensitivity to water content should be further explored in both global and focal cerebral edema models to more fully characterize cerebral edema progression.

Overall, the results of these studies demonstrate that OCT is sensitivity to optical changes caused by cytotoxic and vasogenic edema formation *in vivo.* The global model of edema presented in Chapter 2 was a pure cytotoxic edema model. Histological analysis in the TBI experiments in Chapter 3 confirmed vasogenic edema formation. However, edema formation following TBI typically has components of both vasogenic and cytotoxic edema. Future studies could investigate differences between the optical changes caused by cytotoxic and vasogenic edema by comparing the water intoxication studies to *in vivo* cortical freeze injury, which is a purely vasogenic edema model. The scattering and absorption from each type of edema could be measured using DA-OCT and compared to local tissue biopsy measurements of water content and histological analysis. The ability to differentiate the two types of brain swelling would be useful both clinically and also for studying the effects of various treatments on each type of edema, which could further the understanding of time dynamics and interplay between vasogenic and cytotoxic edema as well as the role of Aquaporin 4 (AQP4) channels in its development.

Additionally, more experiments can be conducted to further investigate the sensitivity of OCT to mTBI. Local tissue biopsy could be taken at various distances away from the impact site to measure the water content using specific gravity and compare the change in water content to the variation in the differential absorption signal. Comparison of OCT and DA-OCT images to MRI in the same animals would also be useful to establish the difference in sensitivity of the two techniques. Different injury models, such as fluid percussion (a diffuse injury model), could also be explored.

Utilizing polarization-sensitive OCT (PS-OCT) may also provide a different mode of contrast with which to detect mTBI. We have conducted preliminary experiments to analyze the change in birefringence of the cerebral cortex following mild CCI (see Appendix). The myelin that surrounds axons is known to exhibit birefringence. Therefore damage to the myelin following injury could decrease the measured birefringence. To date, we have observed some instances of small decreases in birefringence following mild CCI. However, further work can be done to determine the sensitivity of PS-OCT to myelin damage as well as improve the OCT post-processing to remove polarization mode dispersion artifact that could be reducing the sensitivity of the OCT signal to small changes in an already small birefringence measurement in the cerebral cortex.

In summary, the results presented here demonstrate the ability of OCT to detect small variations in the optical scattering and absorption properties of edematous brain tissue, including changes caused by both cytotoxic and vasogenic edema. These findings highlight the potential of OCT for *in vivo* cerebral edema detection as well as the

advantage of using optical measurements for early detection of brain swelling. Further work discussed above can help to characterize the sensitivity of OCT for edema detection and move OCT forward in the field of neuroscience research and applications.

Appendix: Contributions to other OCT projects

In addition to developing OCT as a tool for cerebral edema detection, I explored other applications of OCT that utilized the polarization properties of samples to detect structural properties and changes not discernible from other OCT modes of contrast, such as intensity-based imaging. PS-OCT is a functional extension of OCT that measures the birefringence of sample. Birefringence is an optical property of a material that occurs when the refractive index of a material is dependent on the polarization state of light. During PS-OCT image acquisition the sample is probed with two orthogonal polarization states and the accumulated phase retardation between the two states is calculated as a function of depth and used to quantify the birefringence of a sample. PS-OCT images display the depth-resolved phase retardation on a grayscale colormap map ranging from black, representing a 0^{o} phase retardation, to white, indicating a 180^{o} phase retardation. Highly birefringent material will, therefore, appear with multiple bands of black-to-white transitions while a sample with low birefringence appears as a slow black-to-gray transition over the depth of the sample. A schematic of the PS-OCT system used during the experiments described below is shown in Figure 1. Biological samples with highly organized microstructure typically exhibit some degree of birefringence. The work described this section explored the use of PS-OCT for (A) detecting changes in axonal myelin following mTBI in a mouse model, (B) measuring nerve injury and subsequent recovery in the peripheral nervous system (PNS) and (C) assessing wound healing in skin following a burn injury.

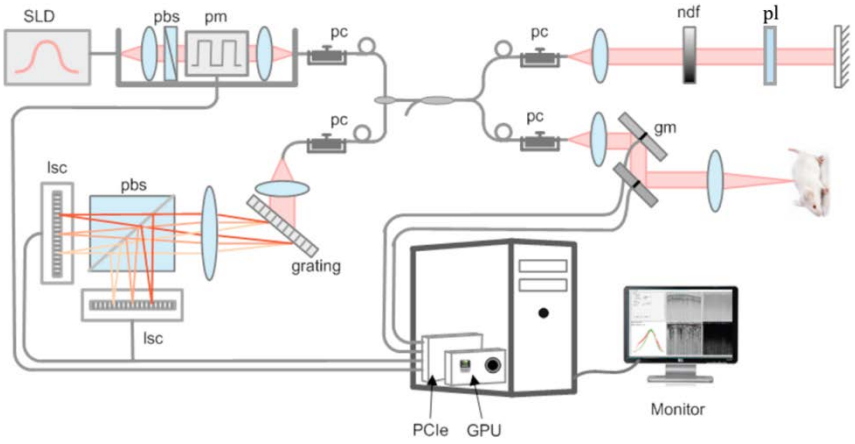

Figure 1. Schematic of PS-OCT system centered at 1300nm. SLD = super-luminescent diode, pbs: polarization beam splitter, pm: polarization modulator, pc: polarization controller, ndf: neutral density filter, pl: polarizer, gm: galvanometer mounted mirrors, lsc: line scan camera, GPU: graphics processing units [58].

A Assessing structural damage following mTBI with PS-OCT

TBI causes structural damage to the brain including axonal injury triggered by the direct force applied to the cranium during impact as well as secondary injuries that develop in the following hours and days. Axons typically grow in very organized directions and are surrounded by a myelin sheath. Both of these factors contribute to a measureable birefringence signal from *in vivo* brain tissue. Therefore, we hypothesize that the measured birefringence following axonal injury should reflect these structural changes.

Preliminary experiments of an mTBI model were conducted using the CCI protocol and imaging parameters described in section 3.2.1. The mouse was prepared with a bilateral craniectomy and imaged with PS-OCT for thirty minutes of baseline recording. CCI was then applied and imaging continued for 1.5 hrs post injury. After imaging was complete, brains were dissected and prepared for immunohistochemistry as

described previously in section 3.2.3. In this case, sagittal sections were cut and stained for myelin basic protein (MBP) to assess myelin damage.

The PS-OCT data were analyzed for changes in accumulated phase retardation following injury in the cerebral cortex. The cerebral cortex exhibited a small but measurable birefringence signal (Figure A.2). In one case, a measurable decrease in the phase retardation was observed following injury (Figure A.2C). The decrease directly at the impact site was slightly more severe compared to a pericontusional site farther from the direct injury. Histological analysis confirmed a loss of myelin in the impacted cortex when compared to a control (Figure A.3).

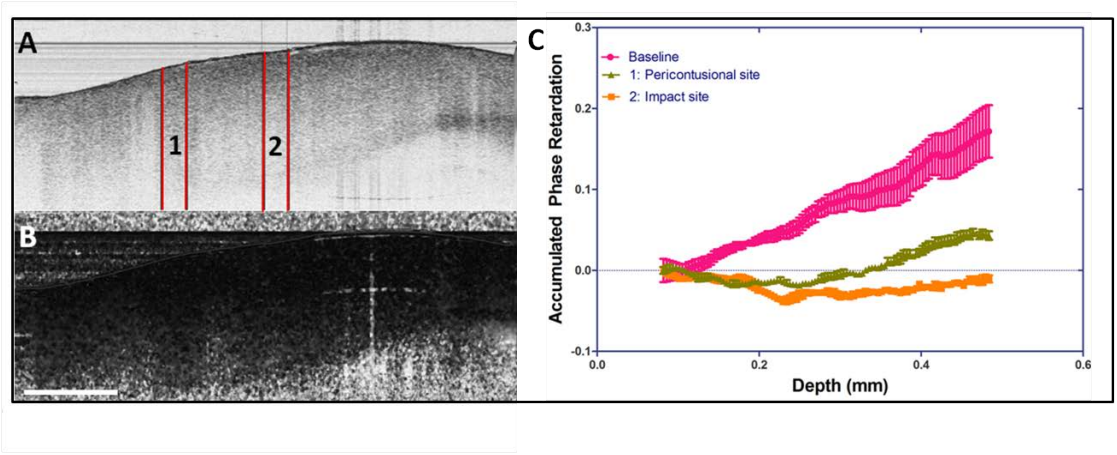

Figure A.2 (A) OCT intensity image of *in vivo* mouse brain following impact and (B) corresponding accumulated phase retardation image. (C) Accumulated phase retardation plots showing the average phase retardation as a function of depth before injury and after injury at both the impact site and pericontusional site at the locations shown in (A). Scale bar = 0.5 mm

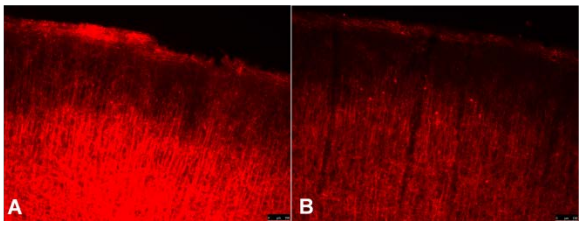

Figure A.3 (A) Myelin basic protein staining in control and (B) following CCI in cerebral cortex, which shows a decrease in myelin compared to the control.

These results demonstrate that OCT has the ability to detect loss of myelin *in vivo* in the cerebral cortex following TBI. However, it should be noted that a decrease in birefringence was not always observed following CCI. Possible explanations for this could be that the current PS-OCT data processing is not sensitive enough to small changes in myelin. Each CCI will be slightly different and the myelin damage may not have been severe enough to always be detected. The PS-OCT post processing can be improved by utilizing a recently published technique to suppress polarization mode dispersion [84], which could be reducing the precision of our measurement and masking subtle changes in phase retardation. Histological analysis on multiple brain samples would need to be done in conjunction with OCT imaging to systematically compare myelin loss and changes in phase retardation.

B Quantitative assessment of peripheral nerve myelination with PS-OCT

A separate project utilized PS-OCT to assess nerve damage and recovery following injury in the PNS. Depending upon the degree of nerve injury, surgical intervention may be

necessary to repair nerve function. Currently never integrity is most commonly assessed by electrical analysis, which does not provide quantitative information regarding function or myelination. The myelin sheath surrounding the axon normally exhibits birefringence. Therefore, in this study we examined the use of PS-OCT to quantitatively assess the myelination changes after nerve injury. The details of this longitudinal study were published in the *Journal of Biomedical Optics* [85] and are summarized below.

A nerve crush injury was applied to the sciatic nerve in a rat model by anesthetizing the animals and exposing the right sciatic nerve via a dorso-lateral muscle splitting incision and then applying a standardized demyelinating crush injury [86]. The site was marked with a single suture to later identify the location of injury for imaging. PS-OCT imaging was performed using a SD-OCT system centered at 1300 nm at the injury site at weeks one, two, three and four following injury by surgically exposing the nerve. A 5 mm x 5 mm area across the crush site was imaged. The uninjured nerve from the contralateral side was also imaged as a control. Walking track analysis was performed at the same time points to assess the degree of injury and subsequent recovery and was quantified by calculating the sciatic function index (SFI) [87]. Animals were divided into four groups ($n = 8$). At each time point, one group was sacrificed and samples of the injured and contralateral uninjured nerves were harvested for histomorphometric analysis of axon diameter and myelin thickness.

Representative OCT data from a control is shown in Figure B.1. Figure B.1A and Figure B.1B are the OCT intensity image and corresponding cumulative phase retardation image, showing the position of the nerve and the muscle surrounding it. The

average depth-resolved phase retardation plot and linear fit is shown in Figure B.1 C. The corresponding histological section is represented in Figure B.1 D, where the dark myelin sheaths surrounding the axons are evident. For comparison, the same data from a representative nerve, one week post injury is shown in Figure B.2.

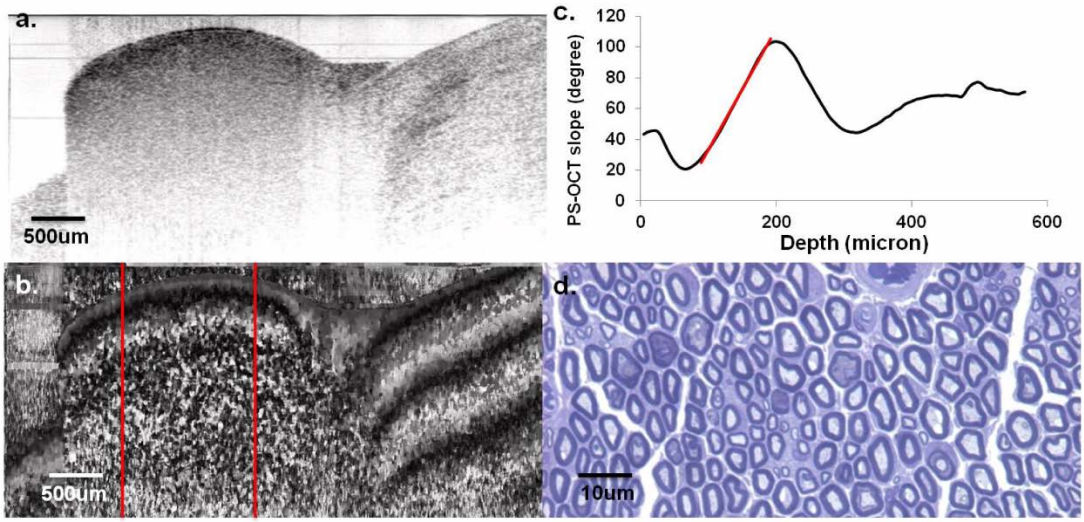

Figure B.1. Normal sciatic nerve: (A) OCT intensity and (B) PS-OCT phase retardation image of nerve and surrounding muscle, (C) plot of average phase retardation as a function of depth (slope of linear fit: $0.4328^{0}/\mu m$) and (D) corresponding histology at 400x.

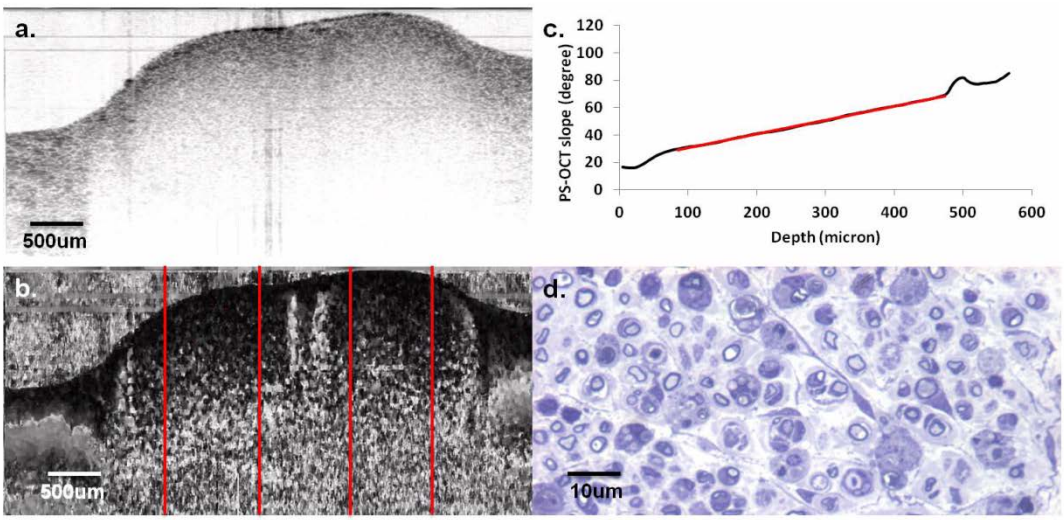

Figure B.2. Sciatic nerve 7 days post-injury: (A) OCT intensity and (B) PS-OCT phase retardation image of nerve and surrounding muscle, (C) plot of average phase retardation as a function of depth (slope of linear fit: $0.0872^0/\mu m$) and (D) corresponding histology at 400x.

Comparison of the PS-OCT slope, which is proportional to the birefringence, to the SFI demonstrate that SFI increased as a function of PS-OCT slope. Although SFI is not specific to myelination, these data show that the nerve crush injury resulted in functional loss and subsequent recovery of the nerve and that PS-OCT slope followed the same increasing trend. The relationship between PS-OCT slope and myelin thickness determined from histomorphometric analysis showed a similar increasing trend with the exception of week 1. The histology revealed that myelin degeneration occurs through week 2, at which point the myelin thickness reached its smallest value. In contrast, the PS-OCT slope was smallest during week 1, suggesting that degenerating myelin does not contribute to the measured birefringence and thus PS-OCT slope can be used to provide a more accurate measure of viable myelin thickness and integrity during early time points.

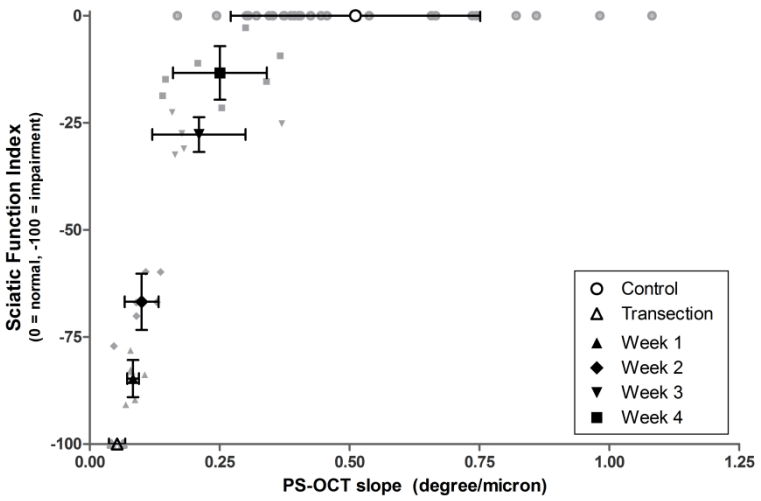

Figure B. 3 SFI versus PS-OCT slope. Both SFI and PS-OCT increase with time post-injury

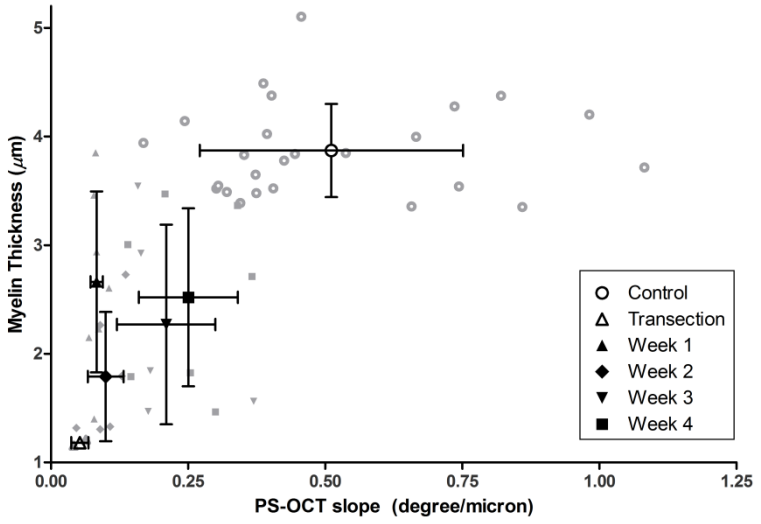

Figure B. 4 Myelin thickness versus PS-OCT slope. Myelin degeneration occurred through week 2, followed by myelin regeneration.

The results of this study demonstrated a loss of nerve function following crush injury and the subsequent recovery of function in the following weeks. The non-contact optical measurement of neural myelination, quantified by PS-OCT slope, followed a

similar increasing trend, demonstrating the use of PS-OCT for assessment of axonal myelination and neuron function. OCT can provide an *in vivo*, non destructive measure of axonal myelination which shows great promise for its continued used both clinically and experimentally in the field of neuroscience.

C Measuring wound healing with PS-OCT

Collagen is a structural protein commonly found in fibrous tissues including skin, tendons and cartilage. It exists in elongated fibers which are highly aligned and organized, causing these structures to exhibit form birefringence. When a burn occurs on the skin, a complex healing process is set in motion during which the damaged collagen undergoes degradation and new collagen is subsequently deposited. In this study, we investigated the use of PS-OCT to quantify the rate of burn wound healing following a treatment with an alginate sponge dressing (ASD) containing insulin encapsulated in PLGA microparticles. In a previous study, this treatment was shown to cause increased collagen deposition and maturation that exhibited a more organized, basket wave form compared to control.

A partial thickness burn wound was made on the dorsum of anesthetized rats using a brass cylinder (1.5 cm diameter) heated in a 80°C water bath for 2 minutes and pressed against the skin for 6 seconds. Following the burn, animals were positioned in the sample arm of our PS-OCT system. Three regions, each covering a 3 mm x 3 mm area inside the boundary of the original burned area, were imaged. The first area covered the center of the burn. The second was directly next to the center, covering a “middle”

region and the third neighbored the middle region and extended to the edge of the burn. Normal, unburned skin approximately 2-3 cm away from burn site was also imaged as control. The same locations were repeatedly imaged on days 1, 3, 6, 9, 12, 15 and 18. Following imaging on day 0, wounds were dressed with either the insulin treatment or a saline control treatment ($n = 8$ for each group). Dressings were changed every three days. All procedures and protocols were approved by the University of California Riverside Institutional Animal Care and Use Committee.

The mean accumulated phase retardation was determined as a function of depth from each imaging region in each rat by calculating the average of 20 measurements, each made up of 500 A-lines, throughout the PS-OCT imaging volume. The data was then fit to a line. The slope of this line was used to quantify the rate of healing, as this value is proportional to the birefringence of the sample. The results are shown in Figure C. 1.

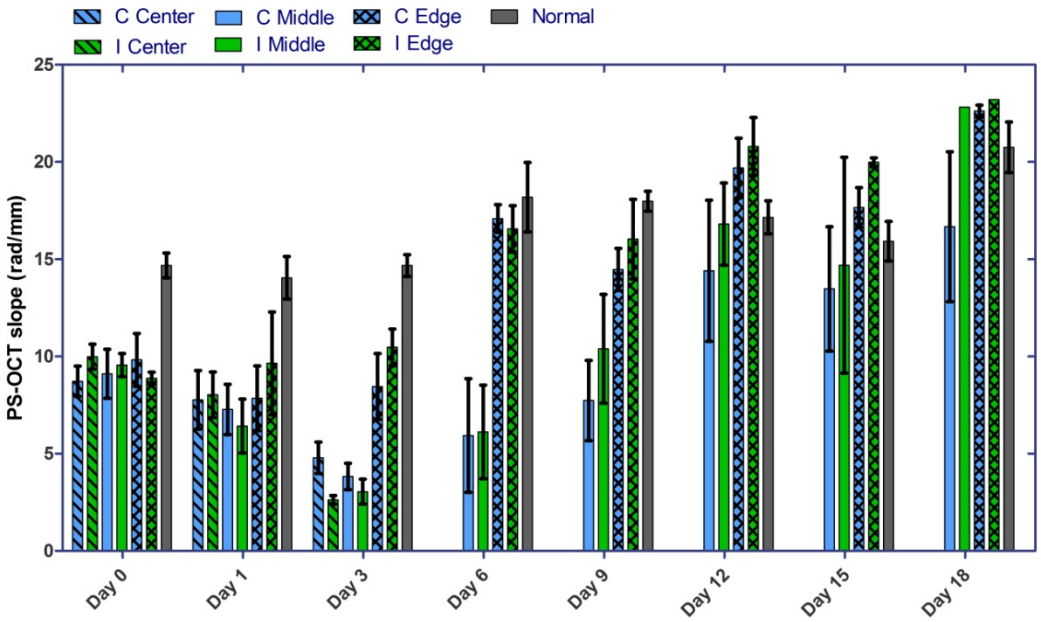

Figure C. 1 PS-OCT slope as a function of time for insulin treated group and control group at various imaging sites.

The overall trend in all of the imaged areas showed an initial decrease in PS-OCT slope, due to collagen degradation, followed by an increase as the wounds heal. The edge regions healed first, followed by the middle. It should be noted that by day 6, the wounds formed thick scabs that did not contain any measureable SNR in the OCT image. Therefore, the center regions were excluded from later time points. Small differences were observed between the two treatment groups. While both groups demonstrated collagen degradation between day 0-3, by day 3 both the middle and center region for the insulin group had lower average slopes compared to control, indicating quicker degradation of collagen and/or better clearance of collagen.

These preliminary results demonstrate that PS-OCT is capable of detecting the time course of collagen degradation and reformation following a burn injury and suggest

that PS-OCT could be used as a tool for measuring the rate of wound healing *in vivo*. Comparison of these results to histological analysis of the collagen structure and network at each time point could help to further interpret these results and is currently being investigated. Similarly, the use of DA-OCT for detection of edema following the burn could be beneficial for understanding how the insulin treatment effects edema formation and progression.

References

1. D. Huang, E. A. Swanson, C. P. Lin, J. S. Schuman, W. G. Stinson, W. Chang, M. R. Hee, T. Flotte, K. Gregory, C. A. Puliafito, and J. G. Fujimoto, "Optical Coherence Tomography," Science (80-.). **254**, 1178–1181 (1991).

2. J. G. Fujimoto, C. Pitris, S. a Boppart, and M. E. Brezinski, "Optical coherence tomography: an emerging technology for biomedical imaging and optical biopsy.," Neoplasia **2**, 9–25 (2000).

3. J. G. Fujimoto, "Optical coherence tomography for ultrahigh resolution in vivo imaging.," Nat. Biotechnol. **21**, 1361–7 (2003).

4. W. Jung and S. a Boppart, "Optical coherence tomography for rapid tissue screening and directed histological sectioning.," Anal. Cell. Pathol. (Amst). **35**, 129–143 (2011).

5. M. R. Hee, J. A. Izatt, E. A. Swanson, D. Huang, J. S. Schuman, C. P. Lin, C. A. Puliafito, and J. G. Fujimoto, "Optical coherence tomography of the human retina.," Arch. Ophthalmol. **113**, 325–332 (1995).

6. J. A. Goldsmith, Y. Li, M. R. Chalita, V. Westphal, C. A. Patil, A. M. Rollins, J. A. Izatt, and D. Huang, "Anterior chamber width measurement by high-speed optical coherence tomography," Ophthalmology **112**, 238–244 (2005).

7. M. Wojtkowski, R. Leitgeb, A. Kowalczyk, T. Bajraszewski, and A. F. Fercher, "In vivo human retinal imaging by Fourier domain optical coherence tomography.," J. Biomed. Opt. **7**, 457–463 (2002).

8. I.-K. Jang, G. J. Tearney, B. MacNeill, M. Takano, F. Moselewski, N. Iftima, M. Shishkov, S. Houser, H. T. Aretz, E. F. Halpern, and B. E. Bouma, "In vivo characterization of coronary atherosclerotic plaque by use of optical coherence tomography.," Circulation **111**, 1551–1555 (2005).

9. I.-K. Jang, B. E. Bouma, D.-H. Kang, S.-J. Park, S.-W. Park, K.-B. Seung, K.-B. Choi, M. Shishkov, K. Schlendorf, E. Pomerantsev, S. L. Houser, H. T. Aretz, and G. J. Tearney, *Visualization of Coronary Atherosclerotic Plaques in Patients Using Optical Coherence Tomography: Comparison with Intravascular Ultrasound.* (2002), Vol. 39.

10. H. Yabushita, "Characterization of Human Atherosclerosis by Optical Coherence Tomography," Circulation **106**, 1640–1645 (2002).

11. B. H. Park, C. Saxer, S. M. Srinivas, J. S. Nelson, and J. F. de Boer, "In vivo burn depth determination by high-speed fiber-based polarization sensitive optical coherence tomography.," J. Biomed. Opt. **6**, 474–479 (2001).

12. M. C. Pierce, J. Strasswimmer, B. H. Park, B. Cense, and J. F. de Boer, *Advances in Optical Coherence Tomography Imaging for Dermatology*. (2004), Vol. 123.

13. S. A. Boppart, "Optical coherence tomography: technology and applications for neuroimaging.," Psychophysiology **40**, 529–41 (2003).

14. A. F. Fercher, C. K. Hitzenberger, G. Kamp, and S. Y. Elzaiat, "Measurement of intraocular distances by backscattering spectral interferometry," Opt. Commun. **117**, 43–348 (1995).

15. J. F. De Boer, B. Cense, B. H. Park, M. C. Pierce, G. J. Tearney, and B. E. Bouma, "Improved signal-to-noise ratio in spectral-domain compared with time-domain optical coherence tomography," Opt. Lett. **28**, 2067–2069 (2003).

16. M. Choma, M. Sarunic, C. Yang, and J. Izatt, "Sensitivity advantage of swept source and Fourier domain optical coherence tomography.," Opt. Express **11**, 2183–2189 (2003).

17. R. Leitgeb, C. Hitzenberger, and A. Fercher, "Performance of fourier domain vs. time domain optical coherence tomography.," Opt. Express **11**, 889–94 (2003).

18. W. Drexler and J. G. Fujimoto, *Optical Coherence Tomography: Technology and Applications* (Springer Science and Business Media, 2008).

19. G. Häusler, "Coherence Radar" and "Spectral Radar"—New Tools for Dermatological Diagnosis," J. Biomed. Opt. **3**, 21–31 (1998).

20. K. K. H. Chan, "Spectral Domain Optical Coherence Tomography System Design : Sensitivity Fall-off and Processing Speed Enhancement by," The University of British Columbia (2010).

21. N. A. Nassif, B. Cense, B. H. Park, M. C. Pierce, S. H. Yun, B. E. Bouma, G. J. Tearney, and T. C. Chen, "In vivo high-resolution video-rate spectral-domain optical coherence tomography of the human retina and optic nerve," Opt. Express **12**, (2004).

22. M. Mujat, B. H. Park, B. Cense, T. C. Chen, and J. F. de Boer, "Autocalibration of spectral-domain optical coherence tomography spectrometers for in vivo

quantitative retinal nerve fiber layer birefringence determination.," J. Biomed. Opt. **12**, 041205 (2013).

23. M. Wojtkowski, V. Srinivasan, T. Ko, J. Fujimoto, A. Kowalczyk, and J. Duker, "Ultrahigh-resolution, high-speed, Fourier domain optical coherence tomography and methods for dispersion compensation.," Opt. Express **12**, 2404–2422 (2004).

24. S. Yun, G. Tearney, B. Bouma, B. Park, and J. de Boer, "High-speed spectral-domain optical coherence tomography at 1.3 mum wavelength.," Opt. Express **11**, 3598–604 (2003).

25. Z. Hu, Y. Pan, and A. M. Rollins, "Analytical model of spectrometer-based two-beam spectral interferometry.," Appl. Opt. **46**, 8499–505 (2007).

26. J. a Izatt, M. D. Kulkarni, S. Yazdanfar, J. K. Barton, and A. J. Welch, "In vivo bidirectional color Doppler flow imaging of picoliter blood volumes using optical coherence tomography.," Opt. Lett. **22**, 1439–41 (1997).

27. Y. Zhao, Z. Chen, C. Saxer, S. Xiang, J. F. de Boer, and J. S. Nelson, "Phase-resolved optical coherence tomography and optical Doppler tomography for imaging blood flow in human skin with fast scanning speed and high velocity sensitivity.," Opt. Lett. **25**, 114–6 (2000).

28. H. Ren, K. M. Brecke, Z. Ding, Y. Zhao, J. S. Nelson, and Z. Chen, "Imaging and quantifying transverse flow velocity with the Doppler bandwidth in a phase-resolved functional optical coherence tomography.," Opt. Lett. **27**, 409–411 (2002).

29. Y. Wang, "Development and Applications of 4D Real-Time Multi-Functional Spectral-Domain Optical Coherence Tomography," University of California Riverside (2013).

30. J. F. de Boer, T. E. Milner, M. J. van Gemert, and J. S. Nelson, "Two-dimensional birefringence imaging in biological tissue by polarization-sensitive optical coherence tomography.," Opt. Lett. **22**, 934–936 (1997).

31. B. H. Park, M. C. Pierce, B. Cense, and J. F. de Boer, "Jones matrix analysis for a polarization-sensitive optical coherence tomography system using fiber-optic components.," Opt. Lett. **29**, 2512–2514 (2004).

32. B. H. Park, M. C. Pierce, B. Cense, and J. F. de Boer, "Optic axis determination accuracy for fiber-based polarization-sensitive optical coherence tomography.," Opt. Lett. **30**, 2587–2589 (2005).

33. S. A. Boppart, B. E. Bouma, M. E. Brezinski, G. J. Tearney, and J. G. Fujimoto, "Imaging developing neural morphology using optical coherence tomography.," J. Neurosci. Methods **70**, 65–72 (1996).

34. S. A. Boppart, M. E. Brezinski, B. E. Bouma, G. J. Tearney, and J. G. Fujimoto, "Investigation of developing embryonic morphology using optical coherence tomography.," Dev. Biol. **177**, 54–63 (1996).

35. N. Sudheendran, S. Bake, R. C. Miranda, and K. V Larin, "Comparative assessments of the effects of alcohol exposure on fetal brain development using optical coherence tomography and ultrasound imaging.," J. Biomed. Opt. **18**, 20506 (2013).

36. C.-P. Liang, J. Wierwille, T. Moreira, G. Schwartzbauer, M. S. Jafri, C.-M. Tang, and Y. Chen, "A forward-imaging needle-type OCT probe for image guided stereotactic procedures.," Opt. Express **19**, 26283–94 (2011).

37. H. Wang, A. J. Black, J. Zhu, T. W. Stigen, M. K. Al-Qaisi, T. I. Netoff, A. Abosch, and T. Akkin, "Reconstructing micrometer-scale fiber pathways in the brain: multi-contrast optical coherence tomography based tractography.," Neuroimage **58**, 984–92 (2011).

38. H. Wang, J. Zhu, and T. Akkin, "Serial optical coherence scanner for large-scale brain imaging at microscopic resolution," Neuroimage **84**, 1007–1017 (2014).

39. H. Wang, J. Zhu, M. Reuter, L. N. Vinke, A. Yendiki, D. A. Boas, B. Fischl, and T. Akkin, "Cross-validation of serial optical coherence scanning and diffusion tensor imaging: A study on neural fiber maps in human medulla oblongata," Neuroimage **100**, 395–404 (2014).

40. B. W. Graf, T. S. Ralston, H.-J. Ko, and S. A. Boppart, "Detecting intrinsic scattering changes correlated to neuron action potentials using optical coherence imaging.," Opt. Express **17**, 13447–13457 (2009).

41. M. M. Eberle, C. L. Reynolds, J. I. Szu, Y. Wang, A. M. Hansen, M. S. Hsu, M. S. Islam, D. K. Binder, and B. H. Park, "In vivo detection of cortical optical changes associated with seizure activity with optical coherence tomography.," Biomed. Opt. Express **3**, 2700–6 (2012).

42. Y. Chen, A. D. Aguirre, L. Ruvinskaya, A. Devor, D. a Boas, and J. G. Fujimoto, "Optical coherence tomography (OCT) reveals depth-resolved dynamics during functional brain activation.," J. Neurosci. Methods **178**, 162–73 (2009).

43. U. M. Rajagopalan and M. Tanifuji, "Functional optical coherence tomography reveals localized layer-specific activations in cat primary visual cortex in vivo.," Opt. Lett. **32**, 2614–2616 (2007).

44. X. L. Faul M, Wald MM, and C. Vg., "Traumatic brain injury in the United States: emergency department visits, hospitalizations, and deaths," in *Centers for Disease Control and Prevention, National Center for Injury Prevention and Control* (2010).

45. H. K. Kimelberg, " Review : Cell Volume in the CNS: Regulation and Implications for Nervous System Function and Pathology," Neurosci. **6**, 14–25 (2000).

46. J. M. Simard, T. a Kent, M. Chen, K. V Tarasov, and V. Gerzanich, "Brain oedema in focal ischaemia: molecular pathophysiology and theoretical implications.," Lancet Neurol. **6**, 258–68 (2007).

47. J. J. Donkin and R. Vink, "Mechanisms of cerebral edema in traumatic brain injury: therapeutic developments.," Curr. Opin. Neurol. **23**, 293–299 (2010).

48. L. C. Padayachy, A. A. Figaji, and M. R. Bullock, "Intracranial pressure monitoring for traumatic brain injury in the modern era.," Child's Nerv. Syst. **26**, 441–52 (2010).

49. M. Czosnyka and J. D. Pickard, "Monitoring and interpretation of intracranial pressure," J. Neurol. Neurosurg. Psychiatry **75**, 813–821 (2004).

50. A. Marmarou, "The pathophysiology of brain edema and elevated intracranial pressure.," Cleve. Clin. J. Med. **71 Suppl 1**, S6–8 (2004).

51. A. A. Rabinstein, "Treatment of cerebral edema.," Neurologist **12**, 59–73 (2006).

52. J. R. Thiagarajah, M. C. Papadopoulos, and A. S. Verkman, "Noninvasive early detection of brain edema in mice by near-infrared light scattering.," J. Neurosci. Res. **80**, 293–9 (2005).

53. A. S. Gill, K. F. Rajneesh, C. M. Owen, J. Yeh, M. Hsu, and D. K. Binder, "Early optical detection of cerebral edema in vivo.," J. Neurosurg. **114**, 470–7 (2011).

54. D. Liang, S. Bhatta, V. Gerzanich, and J. M. Simard, "Cytotoxic edema: mechanisms of pathological cell swelling.," Neurosurg. Focus **22**, E2 (2007).

55. J. I. Szu, M. M. Eberle, C. L. Reynolds, M. S. Hsu, Y. Wang, C. M. Oh, M. S. Islam, B. H. Park, and D. K. Binder, "Thinned-skull cortical window technique for in vivo optical coherence tomography imaging," J. Vis. Exp. (2012).

56. J. E. Olson, L. Mishler, and R. V Dimlich, "Brain water content, brain blood volume, blood chemistry, and pathology in a model of cerebral edema.," Ann. Emerg. Med. **19**, 1113–21 (1990).

57. L. Weed and P. McKibben, "Experimental alteration of brain bulk," Am J Physiol. **73**, 194–195 (1919).

58. Y. Wang, C. M. Oh, M. C. Oliveira, M. S. Islam, A. Ortega, and B. H. Park, "GPU accelerated real-time multi-functional spectral-domain optical coherence tomography system at 1300nm," Opt. Express **20**, 14797 (2012).

59. Z. Chen, T. E. Milner, S. Srinivas, X. Wang, a Malekafzali, M. J. van Gemert, and J. S. Nelson, "Noninvasive imaging of in vivo blood flow velocity using optical Doppler tomography.," Opt. Lett. **22**, 1119–21 (1997).

60. B. R. White, M. C. Pierce, N. Nassif, B. Cense, B. H. Park, G. J. Tearney, B. E. Bouma, T. C. Chen, C. St, and J. F. De Boer, "In vivo dynamic human retinal blood flow imaging using ultra-high-speed spectral domain optical Doppler tomography," Opt. Express **11**, 3490–3497 (2003).

61. K. a Vermeer, J. Mo, J. J. a Weda, H. G. Lemij, and J. F. de Boer, "Depth-resolved model-based reconstruction of attenuation coefficients in optical coherence tomography.," Biomed. Opt. Express **5**, 322–37 (2013).

62. G. Harlow, A. C. Cruz, S. Li, N. S. Thakoor, A. C. Bianchi, J. Chen, B. Bhanu, and Z. Yang, "Automated spatial analysis of ARK2: putative link between microtubules and cell polarity," in *2013 IEEE 10th Internation Symposium on Biomedical Imaging: From Nano to Macro* (2013), pp. 910–913.

63. T. R. Frieden, D. Houry, and G. Baldwin, *Report to Congress on Traumatic Brain Injury in the United States: Epidemiology and Rehabilitation.* (2014).

64. B. E. Wojcik, C. R. Stein, K. Bagg, R. J. Humphrey, and J. Orosco, "Traumatic brain injury hospitalizations of U.S. army soldiers deployed to Afghanistan and Iraq.," Am. J. Prev. Med. **38**, S108–16 (2010).

65. T. a Ashman, W. a Gordon, J. B. Cantor, and M. R. Hibbard, "Neurobehavioral consequences of traumatic brain injury.," Mt. Sinai J. Med. **73**, 999–1005 (2006).

66. T. Tsaousides and W. a Gordon, "Cognitive rehabilitation following traumatic brain injury: assessment to treatment.," Mt. Sinai J. Med. **76**, 173–181 (2009).

67. E. M. Kan, E.-A. Ling, and J. Lu, "Microenvironment changes in mild traumatic brain injury.," Brain Res. Bull. **87**, 359–72 (2012).

68. B. Lee and A. Newberg, "Neuroimaging in traumatic brain imaging.," NeuroRx **2**, 372–83 (2005).

69. S. D. Timmons, A.-C. Duhaime, and S. M. Lee, "Mild traumatic brain injury. Introduction.," Neurosurg. Focus **29**, 1 (2010).

70. J. Sword, T. Masuda, D. Croom, and S. a. Kirov, "Evolution of neuronal and astroglial disruption in the peri-contusional cortex of mice revealed by in vivo two-photon imaging," Brain **136**, 1446–1461 (2013).

71. M. C. Morganti-kossmann, M. Rancan, P. F. Stahel, and T. Kossmann, "Inflammatory response in acute traumatic brain injury : a double-edged sword," 101–105 (2002).

72. D. Kushner, "Mild Traumatic Brain Injury: Towrds Understanding Manifestations and Treatment," Arch intern med **158**, 1617–1624 (1998).

73. A. Marmarou, "Pathophysiology of traumatic brain edema: current concepts.," Acta Neurochir. Suppl. **86**, 7–10 (2003).

74. H. J. Feickert, S. Drommer, and R. Heyer, "Severe head injury in children: impact of risk factors on outcome.," J Trauma **47**, 33–8 (1999).

75. A. Marmarou, S. Signoretti, G. Aygok, P. Fatouros, and G. Portella, "Traumatic brain edema in diffuse and focal injury: Cellular or vasogenic?," Acta Neurochir. Suppl. 24–29 (2006).

76. H. G. Belanger, R. D. Vanderploeg, G. Curtiss, and D. L. Warden, "Recent neuroimaging techniques in mild traumatic brain injury.," J. Neuropsychiatry Clin. Neurosci. **19**, 5–20 (2007).

77. M. E. Shenton, H. M. Hamoda, J. S. Schneiderman, S. Bouix, O. Pasternak, Y. Rathi, M. Vu, M. P. Purohit, K. Helmer, I. Koerte, a P. Lin, C.-F. Westin, R. Kikinis, M. Kubicki, R. a Stern, and R. Zafonte, "A review of magnetic resonance imaging and diffusion tensor imaging findings in mild traumatic brain injury.," Brain Imaging Behav. **6**, 137–92 (2012).

78. A. R. Mayer, P. S. F. Bellgowan, and F. M. Hanlon, "Functional magnetic resonance imaging of mild traumatic brain injury.," Neurosci. Biobe **49**, 8–18 (2015).

79. C. Eierud, R. C. Craddock, S. Fletcher, M. Aulakh, B. King-Casas, D. Kuehl, and S. M. Laconte, "Neuroimaging after mild traumatic brain injury: Review and meta-analysis," NeuroImage Clin. **4**, 283–294 (2014).

80. Y. Xiong, A. Mahmood, and M. Chopp, "Animal models of traumatic brain injury.," Nat. Rev. Neurosci. **14**, 128–42 (2013).

81. J. M. Schmitt, S. H. Xiang, and K. M. Yung, "Differential absorption imaging with optical coherence tomography," J. Opt. Soc. Am. **15**, 2288–2296 (1998).

82. M. Pircher, E. Götzinger, R. Leitgeb, A. Fercher, and C. Hitzenberger, "Measurement and imaging of water concentration in human cornea with differential absorption optical coherence tomography.," Opt. Express **11**, 2190–7 (2003).

83. A. Marmarou, W. Poll, K. Shulman, and H. Bhagavan, "A simple gravimetric technique for measurement of cerebral edema.," J. Neurosurg. **49**, 530–7 (1978).

84. M. Villiger, E. Z. Zhang, S. K. Nadkarni, W. Y. Oh, B. J. Vakoc, and B. E. Bouma, "Spectral binning for mitigation of polarization mode dispersion artifacts in catheter-based optical frequency domain imaging," Opt. Express **21**, 16353–16369 (2013).

85. F. P. Henry, Y. Wang, C. L. R. Rodriguez, M. A. Randolph, E. A. Z. Rust, J. M. Winograd, J. F. de Boer, and B. H. Park, "In vivo optical microscopy of peripheral nerve myelination with polarization sensitive-optical coherence tomography," J. Biomed. Opt. **20**, (2015).

86. P. M. Bridge, D. J. Ball, S. E. Mackinnon, Y. Nakao, K. Brandt, D. A. Hunter, and C. Hertl, "Nerve crush injuries--a model for axonotmesis.," Exp. Neurol. **127**, 284–290 (1994).

87. J. R. Bain, S. E. Mackinnon, and D. A. Hunter, "Functional evaluation of complete sciatic, peroneal, and posterior tibial nerve lesions in the rat.," Plast. Reconstr. Surg. **83**, 129–138 (1989).